Investigating chemical and cracking processes in cement paste exposed to a low external sulfate attack with emphasis on the contribution of gypsum

Julie Pouya, Mejdi Neji, Laurent de Windt, Frédéric Péralès, Adrien Socié, Jérôme Corvisier

Investigating chemical and cracking processes in cement paste exposed to a low external sulfate attack with emphasis on the contribution of gypsum

Julie Pouya[a,b], Mejdi Neji[a], Laurent De Windt[b,*], Frédéric Péralès[c], Adrien Socié[b], Jérôme Corvisier[b]

[a] *Institut de Radioprotection et de Sûreté Nucléaire (IRSN), PSE-ENV/SEDRE/LETIS, F-92260, Fontenay-aux-Roses, France*

[b] *Mines Paris, PSL University, Centre for Geosciences and Geoengineering, 35 rue Saint-Honoré, 77300 Fontainebleau, France*

[c] *Institut de Radioprotection et de Sûreté Nucléaire (IRSN), PSN-RES/SEMIA/LSMA, F-13115 Saint-Paul-Lez-Durance, France*

*Corresponding author.
Email addresses:
julie.pouya@irsn.fr (J. Pouya), mejdi.neji@irsn.fr (M. Neji) laurent.de_windt@minesparis.psl.eu (L. De Windt), frederic.perales@irsn.fr (F. Perales), adrien.socie@cea.fr (A. Socie), jerome.corvisier@mines-paristech.fr (J. Corvisier).

Highlights

- Multiple characterization tools were used including a synchrotron radiation CT.
- Contributions of hydrolysis and sulfate attack on damage were discriminated.
- Expansion occurred even for low C_3A content and groundwater SO_4 concentration.
- Cracking was initiated in the gypsum formation zone.
- Ettringite formation was identified by microindentation and homogenization.

Abstract

Durability of concrete exposed to an external sulfate attack is a great concern for the long-term reliability of nuclear waste containment. This paper presents experimental results obtained on cement paste subjected to a low concentration (30×10^{-3} mol/L) external sulfate attack. Samples were characterized with complementary methods (XRD, SEM-EDS, microtomography, microindentation, autoradiography) to follow the evolution of chemical, mineralogical, microstructural and mechanical properties during 8 months. Cement pastes of different C_3A contents were used to boost either ettringite or gypsum formation during the sulfate attack to assess their respective impact on the degradation. Cracks parallel to the attacked surface occurred in the zone of gypsum formation and portlandite dissolution, which suggests that gypsum has a key effect on the expansion. Reactive transport modeling supported the discussion on the competition between hydrolysis, gypsum and ettringite precipitation as well as the analytical homogenization to estimate Young's moduli.

Keywords: CEM I, sulfate attack, gypsum, cracks, modelling, micromechanics.

1. Introduction

Long-term reliability of nuclear waste containment in geologic disposals needs to design concrete structures resistant to chemical environments containing sulfates. Cement-based

materials will be used in the design of the radioactive waste packages as well as for mechanical support of the sealing system of galleries. The natural waters of the geological media contain significant amounts of sulfate that will diffuse into the cementitious porous media, leading to the so-called external sulfate attacks (ESA) [1,2]. ESA consists in the precipitation of secondary ettringite and gypsum due to reaction between sulfate ions and hydrated cement phases. Formation of ettringite and gypsum leads to swelling pressure and, therefore, to cracking, expansion, spalling and loss of strength of the cementitious material [3–5]. Thus, ESA is widely known as a real threat to concrete durability and yet the phenomenology of the reaction still raises questions [6–8]. A two-step degradation process usually takes place. First, no or slight expansion of the sample is observed, then serious deterioration of the material occurs [9].

However, the mechanism which takes part during the first stage leading to a significant expansion remains unclear, partly because this process results from the coupling between chemical reactions, diffusive transport and mechanical behavior of the material [10,11]. Thus, the sample expansion remains the result of multiscale and multiphysic phenomena. One of the establishing facts so far is the expansion and the mechanical damage related to the ettringite formation. The source of expansion remains a debate and the two main theories are based on the one hand on the crystallization pressure [12,13] and on the other hand on the differential molar volume between the sulfate product (ettringite) and the aluminate sources. In some studies, material cracking is exclusively attributed to ettringite precipitation [5,14]. In particular, a correlation between the amount of ettringite formed during the reaction and the level of damage has been pointed out by varying the initial amount of C_3A contained in the cement, which acts as a source of aluminum for ettringite formation. The higher the C_3A content of the cement pastes, the higher the expansion rate [9,15]. Nevertheless, some laboratory tests have shown that ESA damages occurred even for cement containing none or less than 5% of C_3A [16,17], suggesting that secondary ettringite formation is not the only source of expansion.

Similarly, Gonzalez and Irassar [17] have studied sulfate attacks on specimens with low C_3A content but various amounts of C_3S. Greater expansion occurred for materials containing more C_3S, while significant localized gypsum formation was found. Gypsum may be due to the higher amount of portlandite formed during the hydration of cement containing more C_3S [18]. This last point underlines the material effect on both chemical and mechanical behavior that influences the quantity of available reactant as well as the cementitious resistivity. Furthermore, some studies suggested that gypsum formation is more harmful than ettringite precipitation [19,20] and should also be taken into consideration as a factor of damage [21]. However, the exact mechanism of gypsum on expansion remains unclear, and works aiming to identify the damaging effects of gypsum formation during sulfate attacks are still debated. Nonetheless, the ESA is induced by sulfate diffusion inside the cementitious material and the expansion process due to secondary precipitation can take up to several years [14,22].

High sulfate concentrations (e.g. 0.15 – 0.70 mol/L, c. 14500 – 67250 mg/L) are commonly used to accelerate cement degradation [4,14,23]. However, such tests may not be extrapolated to realistic conditions. The sulfate concentrations of groundwaters are generally much lower in many environmental media. In geologic disposal sites or underground research laboratories, the SO_4 porewater total concentration is within 10 – 30 mmol/L (c. 950 – 2900 mg/L) in the Toarcian argillite [24], 10 – 20 mmol/L (c. 950 – 1900 mg/L) in the Callovo-Oxfordian claystone [25] and 7 – 17 mmol/L (c. 650 – 1650 mg/L) in the Opalinus Clay [26]. Natural waters from subsoils or deeper geological formations containing gypsum will also be

contaminated by relatively low concentration in sulfates. The natural dissolution of gypsum in the subsoil can have an impact on the infrastructures. For instance, aqueous concentrations within 12 – 20 mmol/L (c. 1150 – 1900 mg/L) can be found in some subsoils during the subway extension in the Île-de-France region (France) [27]. The concentration of sulfates measured in saline rivers can also be as high as 16 mmol/L (c. 1500 mg/L) [28], which can be detrimental for bridges. It is worth mentioning that the pH of the water with such relatively "low" sulfate concentrations (disposal, subsoil, saline river) is usually close to neutrality (pH 6 – 9).

Furthermore, high sulfate concentrations can lead to mineralogical distribution and expansion initiation different from the one encountered in the context of radioactive waste disposal. High sulfate concentrations also lead to a quick and complete destruction of the cement matrix that complexifies a detailed characterization of the degradation fronts. Another relevant process that may occur during external sulfate attacks is the hydrolysis of cement hydrates for solutions of pH less than the value of the cement porewater (pH around 12.5 in Portland cements). Ca-leaching resulting from portlandite dissolution and C-S-H decalcification contributes to the weakening of the material and should be considered as a consequence of ESA [20,29,30]. However, the contribution of expansive product precipitation vs. hydrolysis to material damage is difficult to estimate, as these reactions occur more or less at the same time and may influence each other.

The present experimental study provides data on the degradation mechanisms of cement pastes subjected to moderate ESA in order to better understand the impact of gypsum formation on the material damage. Hardened/hydrated cement pastes enable the study of degradation at a micron scale, i.e. in the order of magnitude of mineralogical changes. They offer the advantage of easier implementation of characterization tests by SEM-EDS and XRD, unlike mortars and concretes that exhibit heterogeneities due to the presence of aggregates. A preliminary study [31] has considered the degradation of a C_3A-rich hardened CEM I paste (HCP) using a non-renewed solution without pH regulation mimicking a sulfate-confined environment. In this study, both a C_3A-rich paste and a C_3A-poor CEM I were used to promote ettringite or gypsum formation, respectively. Those HCP were immersed in a low-concentration sodium sulfate solution (30×10^{-3} mol/L, i.e. 2900 mg/L) at a constant neutral pH close to the pH found in natural waters. The objective was to compare the degradation of a cement paste in which a significant amount of ettringite was formed with a cement paste containing less ettringite but more gypsum, to discriminate the effect of each mineral on the deterioration of the material. Periodically, samples were extracted for chemo-mechanical characterization. The chemical evolution of samples was investigated by SEM-EDS analyses. Layer-by-layer XRD analyses provided data about mineralogical evolution depending on depth. Microstructural evolution was assessed by microtomography and autoradiography. Nanoindentation determined the impact of ESA on elastic mechanical properties. Reactive transport modeling of the chemical degradation supported the interpretation of experimental results as well as an analytical homogenization scheme to calculated Young's moduli.

2. Materials and methods

2.1. Materials

Two CEM I HCP were casted with different C_3A ratio: C_3A-poor (4%, Le Teil CEM I 52.5 N SR 5 CEM PM-CP2 NF) and C_3A-rich (11%, Beffes CEM I 52.5 N CE CP2 NF). Their

compositions are given in Table 1. Hydration was performed with a water/cement mass ratio of 0.5. The samples were cylinders of 3 cm diameter and, as a result of the cutting process, the samples measure approximately 1 cm in thickness. Both surfaces are in contact with the sulfate solution. Therefore, the maximum degradation depth is 5000 µm (0.5 cm). They were kept in sealed bags at a constant temperature of 20°C for 28 days. The samples were protected from lateral degradation by a resin epoxy Resoltech 3030 coating, such that ESA occurred in one direction only, perpendicularly to the circular faces.

The samples contained one or two built-in cracks at their center (Fig.1a). However, it is important to note that the investigation discussed in this paper does not involve the pre-existing cracks. They were created to study the impact of pre-cracking on degradation during an ESA. To ensure the accuracy of the analysis within the scope of this paper's study, visual inspection and the solid analytical methods detailed below enabled to select analyzing zones of the hydrated cement pastes that were located at a distance far enough from the initial crack not to be impacted by it, as schematically shown in Fig. 1b.

Table 1. Cement compositions.

	C_3A-poor CEM I	C_3A-rich CEM I
Chemical analysis (g/100 g)		
Loss on ignition	1.3	2.9
SiO_2	22.8	19.3
Al_2O_3	2.7	5.3
Fe_2O_3	1.8	2.60
CaO	67.4	63.2
SO_3	2.23	3.5
Na_2O	0.14	0.08
K_2O	0.37	0.94
Normative phase composition (g/100 g)		
C_3A	4	11
C_3S	66	66
C_2S	18	10
C_4AF	7	8
$CaCO_3$	3	4
Water		
W/C (mass)	0.5	0.5

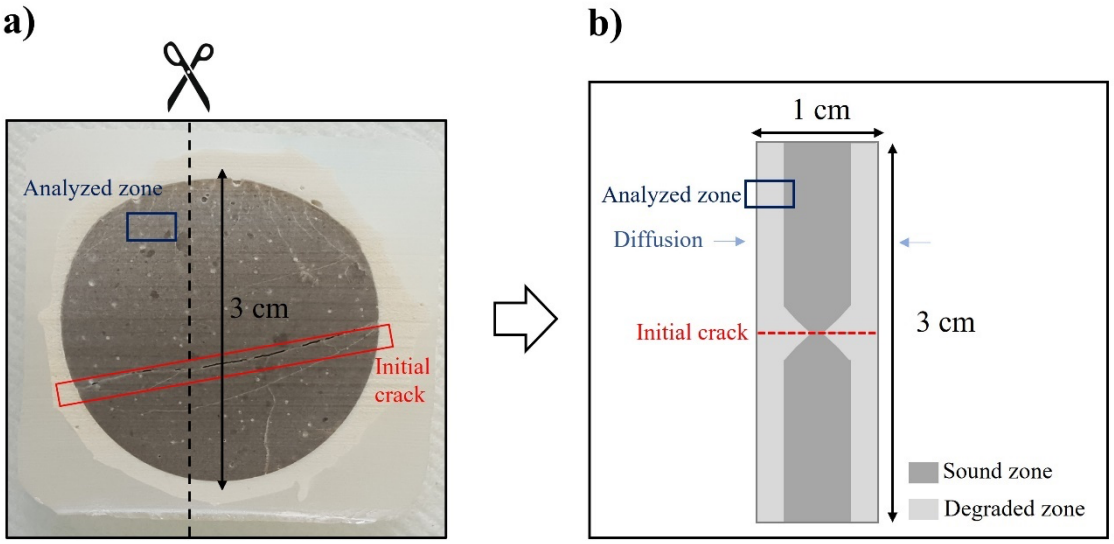

Fig. 1. Degraded pre-cracked sample (a). The sample was cut perpendicularly to the initial crack to obtain a polished section as shown in (b). The experimentally characterized zone was located at a distance far enough from the initial crack not to be impacted by it.

2.2. Experimental setup

Five cylindric samples of each type of cement were placed in two different tanks of 60 L at room temperature. The tanks were filled with a Na_2SO_4 solution at 30×10^{-3} mol/L. Solution volumes were large enough to globally maintain a constant chemical composition over time, but the pH had to be manually fixed between 7 and 9 by adding nitric acid HNO_3. Controlling the pH within the neutral pH range (pH 7 - 9) was ensured by adding rather small amounts of nitric acid, which is not equivalent to studies devoted to acid attack by HNO_3 with much higher acid concentration. The advantage of HNO_3 is that the nitrates (NO_3^-) salts present a high solubility and, therefore, have no or minimal disruptive effect on the cement paste.

The tanks were sealed after nitrogen gas injection to avoid carbonation. Samples were collected after 0.5, 2, 4 and 6 months to be analyzed.

2.3. Characterization techniques of degraded samples

2.3.1. X-ray diffraction

X-ray diffraction (XRD) analyses were performed to follow the mineralogical variation as a function of depth and time. Acquisition was made directly on the solid [32,33]. Between each measurement, a layer of about 150 µm thick was removed with abrasive paper from the external surface to the center of the paste, parallel to the attacked surface. A caliper rule was used to control the thickness of the scraped layer. A diffractometer PANalytical Aeris Research Edition was used to collect mineralogical data relying on CuKα radiation (λ = 1.5405 Å), with a working voltage of 40 kV and an intensity equal to 15 mA. The XRD patterns were obtained by exposing the polished surface to the X-ray beam directly, for an angular range from 5° to 70° with a step size of 0.01°. The total acquisition time was 20 minutes. COD database was used for phase identification [34].

2.3.2. Scanning electron microscopy

The chemical element distribution in the cement matrix during the ESA was characterized by scanning electron microscopy (SEM). A Hitachi S3500N SEM was equipped with two energy-dispersive spectrometry (EDS) Brücker SDD detectors to determine the chemical composition of both sound and degraded zones. Samples were first embedded in epoxy resin. Then, polished thin sections were prepared and coated by carbon. The analyses were performed under a voltage of 15 keV at a working distance of 16.7 mm. The spot size of the EDS measurement was approximately 1.5 µm and the SEM-Beam interaction pear was about 3 µm in depth. The software ESPRIT (Bruker) was used for spectrum and EDS map acquisition. Hyperspectral images acquirement was done at 8s per pixel. The spectrum corresponding to gypsum had been identified (Fig. 2) to detect this mineral from the EDS elementary maps.

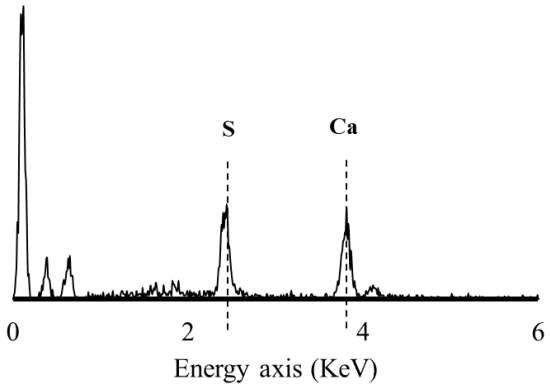

Fig. 2. Spectrum of reference to detect gypsum by SEM-EDS.

2.3.3. X-ray microtomography

X-ray microtomography analyses were performed shortly after removing the sample from the solution, without any drying and epoxy embedding. A computed tomography scanner Brüker SkyScan 1173 was used, equipped with a 2k detector pixels working at 100 keV and 61 µm. Acquisitions were performed with a 360° rotation at step of 0.1°, frame averaging of 16, voxel size of 4 µm. A median filter of radius 2 was applied after data reconstruction. A K-means deconvolution [35] was eventually performed to threshold the 3D reconstructed data, in order to distinguish zones of different densities within the sample.

A computed tomography (CT) scan was also performed on the C_3A-poor cement paste degraded during 8 months with the beamline Anatomix at the French synchrotron Soleil [36]. Acquisition was done with a number of pixels of 2048, horizontally and vertically, with a pixel size of 0.65. The rotation step was 0.09 and a paganin filter was used. About 2000 projection files were generated.

2.3.4. Microindentation

Microindentation analysis was performed by using Anton Paar NHT3 Nanoindenter equipped with Berkovich diamond indenter and coupled to a Step 700 stabilization platform. The aim was to determine the evolution of the Young's modulus of the degraded paste as a function of depth. Acquisition was made on the polished sections prepared for SEM-EDS analysis. The

indenter was vertically pressed into the sample surface, its displacement was monitored, and the corresponding load was measured. The corresponding curve displaying displacement versus load was interpreted to calculate the elastic modulus of indented zones. The elastic modulus values of the material at the indented zone were estimated via Oliver and Phar approach [37]. Adapted indentation parameters were chosen in a way to consider the roughness differences between the sound and degraded zones which could conduct to unreliable elastic modulus values. The load was first raised from 0 to 100 mN with a constant loading rate of 100 mN/min, then maintained constant for 10 sec at the maximum value to limit creep phenomena and, finally, decreased to 0 with an unloading rate of 100 mN/min. The acquisition rate was 15 Hz, the approach distance and speed were 8500 nm and 24000 nm/min, respectively. A grid of 8×8 array of indentation points was adopted with a distance of 300 µm between each other to perform a statistical analysis of measured mechanical values. According to Constantinides et al. [38], the distance between each point should be 10 times greater than maximum displacement before unloading to avoid interaction between neighboring points.

2.3.5. 14C-PMMA autoradiography

The total connected porosity was estimated by the 14C-PMMA autoradiography technique. The latter is based on the measurement of radiation coming from 14C-labelled tracer compound 14C-MMA (MethylMethAcrylate) impregnated in the sample and filling the connected porosity [39,40]. The method consists of impregnating a sample with liquid 14C-labelled methylmethacrylate (14C-MMA) monomer, allowing polymerization of the monomer within the pore space, and subsequently performing autoradiography on the impregnated sample after sawing and polishing. For this purpose, samples of 1 cm width, height and depth were cut, freeze-dried for 2 days and impregnated under vacuum to ensure that the tracer can enter all the pores. The tracer was left to enter the sample pore space during 1 month. Polymerisation into PMMA (PolyMethylMethAcrylate) was performed by gamma irradiation from a 60Co source. Samples were exposed on a photographic film sensitive to β radiation [41] after being cut and polished. The image produced was a 2D connected porosity map of the studied section. Analyses were performed in the Department of Chemistry, Helsinki University (Finland).

2.4. Modeling approach and data

2.4.1. Reactive transport equation

The modeling of the ESA tests was performed with the reactive transport code HYTEC [42]. Under the present water-saturated conditions, the coupling between chemistry and diffusive transport was modeled by the following equation [42]:

$$\frac{\partial \phi c_i}{\partial t} = \nabla \cdot (D_e(\phi) \nabla c_i) - \frac{\partial \phi \overline{c_i}}{\partial t} \qquad (1)$$

where D_e represents the effective diffusion coefficient for all the dissolved species, ϕ is the material total porosity, and c_i and $\overline{c_i}$ are the species i mobile total concentration in solution and immobile total concentration in solid phases, respectively.

Mineral dissolution and precipitation can change the porosity and thus transport properties. The feedback of chemistry on transport was considered by correcting the effective diffusion coefficient D_e according to a modified version of Archie's law [42]:

$$D_e(\phi) = D_e(\phi_0)\left(\frac{\phi - \phi_c}{\phi_0 - \phi_c}\right)^{\alpha} \quad (2)$$

where α is an empirical coefficient usually equal to 3 for cementitious materials [43], ϕ_0 is the initial porosity, and ϕ_c is a threshold under which diffusion stops (set to zero in the present modeling).

2.4.2. Chemical and physical data

All chemical reactions were modeled at local thermodynamic equilibrium with the B-dot activity correction model relevant for ionic strengths up to 1 molal typical of CEM I young pastes. The 2019 version of Thermoddem thermodynamic database was used [44]. All the phases considered during the modeling and their properties are given in Table 2. The progressive C-S-H decalcification was modeled with a discretized set of decreasing Ca/Si ratio. Gypsum, monosulfoaluminate, hemicarboaluminate, calcite, amorphous silica and gibbsite, which could also be formed during the reaction, were included in addition to the primary solid phases.

Table 2. Thermodynamic formation constants at chemical equilibrium and mechanical properties of the solid phases considered in geochemical modelling.

Solid phase	Chemical equation	Log K[(a)] 25°C	Density[(a)] (kg/m^3)	Young Mod. [(b)] (GPa)	Poisson coeff. [(b)]
Cement hydrates					
C1.6SH	$3.2Ca^{2+}+2H_4SiO_4+2.6128H_2O-6.4H^+ \rightarrow (CaO)_{3.2}(SiO_2)_2(H_2O)_{3.4128}$	-55.99	2506	23.8[(2)]	0.24
C1.5SH	$3Ca^{2+}+2H_4SiO_4+2.2631H_2O-6H^+ \rightarrow (CaO)_3(SiO_2)_2(H_2O)_{3.2631}$	-51.44	2478	21.4[(2)]	0.24
C1.4SH	$2.8Ca^{2+}+2H_4SiO_4+1.9144H_2O-5.6H^+ \rightarrow (CaO)_{2.8}(SiO_2)_2(H_2O)_{3.1144}$	-46.93	2447	18.9[(2)]	0.24
C1.3SH	$2.6Ca^{2+}+2H_4SiO_4+1.5659H_2O-5.2H^+ \rightarrow (CaO)_{2.6}(SiO_2)_2(H_2O)_{2.9659}$	-42.47	2415	16.5[(2)]	0.24
C1.2SH	$2.4Ca^{2+}+2H_4SiO_4+1.1895H_2O-4.8H^+ \rightarrow (CaO)_{2.4}(SiO_2)_2(H_2O)_{2.7895}$	-38.09	2389	14.1[(2)]	0.24
C1.1SH	$2.2Ca^{2+}+2H_4SiO_4+0.7491H_2O-4.4H^+ \rightarrow (CaO)_{2.2}(SiO_2)_2(H_2O)_{2.5491}$	-33.76	2380	11.7[(2)]	0.24
C1SH	$2Ca^{2+}+2H_4SiO_4+0.3978H_2O-4H^+ \rightarrow (CaO)_2(SiO_2)_2(H_2O)_{2.3978}$	-29.47	2358	9.2[(2)]	0.24
C0.9SH	$1.8Ca^{2+}+2H_4SiO_4+0.1062\ H_2O-3.6H^+ \rightarrow (CaO)_{1.8}(SiO_2)_2(H_2O)_{2.3062}$	-25.25	2327	6.7[(2)]	0.24
C0.8SH	$1.6\ Ca^{2+}+2H_4SiO_4-0.218H_2O-3.2H^+ \rightarrow (CaO)_{1.6}(SiO_2)_2(H_2O)_{2.182}$	-21.18	2299	4.3[(2)]	0.24
C0.7SH	$1.4Ca^{2+}+2H_4SiO_4-0.6724\ H_2O-2.8H^+ \rightarrow (CaO)_{1.4}(SiO_2)_2(H_2O)_{1.9276}$	-17.80	2292	4.3[(2)]	0.24
Ettringite	$2Al^{3+} + 6Ca^{2+} + 3SO_4^{2-} + 38H_2O \rightarrow Ca_6Al_2(SO_4)_3(OH)_{12}\cdot(H_2O)_{26}(H^+)_{12}$	-57.00	1767 (2500[(1)])	22.4	0.25
Portlandite	$Ca^{2+} + 2H_2O \rightarrow Ca(OH)_2 + 2H^+$	-22.81	2241	42.3	0.324

Monocarbo-aluminate	$2Al^{3+} + 4Ca^{2+} + HCO_3^- + 16.7\,H_2O \rightarrow Ca_4Al_2(CO_3)(OH)_{12} + 13H^+$	-80.55	2148	42.3	0.324
Hemicarbo-aluminate	$4Al^{3+} + 8Ca^{2+} + HCO_3^- + 35\,H_2O \rightarrow Ca_4Al_2(CO_3)(OH)_{12} + 27H^+$	-183.65	1921	-	-
Monosulfo-aluminate	$2Al^{3+} + 4Ca^{2+} + SO_4^{2-} + 18H_2O \rightarrow Ca_4Al_2(SO_4^{2-})(OH)_{12} + 12H^+$	-73.06	2000	42.3	0.324
Other phases					
Gypsum	$Ca^{2+} + SO_4^{2-} + 2H_2O \rightarrow CaSO_4(H_2O)_2$	4.61	2305	45.7	0.33
Calcite	$Ca^{2+} + HCO_3^- \rightarrow CaCO_3 + H^+$	-1.85	2710	79.6	0.31
Gibbsite(3)	$Al^{3+} + 3H_2O \rightarrow Al(OH)_3 + 3H^+$	-7.73	2441	-	-
Microcrystal. $Al(OH)_3$	$Al^{3+} + 3H_2O \rightarrow Al(OH)_3 + 3H^+$	-9.35	2441	-	-
Amorphous silica(3)	$SiO_2(aq) \rightarrow SiO_2(am)$	2.69	2072	-	-

(a)[44], (b) [45]. (1) Density adjusted to the C-S-H one in the reactive transport simulations (see text in Sec. 3.3); (2) Calculated values (see text in Sec. 3.4.1); (3) Crystalline or microcrystalline Al hydroxide was alternately considered in combination with amorphous SiO_2 to try to simulate the Al-Si gel formation (see text in Sec. 3.3).

The anhydrous phases (C_3S, C_2S, C_3A and C_4AF) properties were also considered in the homogenization calculations. The Young's modulus and Poisson ratio of each phase are respectively 117.6 GPa and 0.314 [45].

2.4.3. Initial state and configuration of the cement pastes

XRD analyses indicated that both cement pastes contained portlandite, ettringite, C-S-H and monocarboaluminate. The initial contents in hydrated cement pastes were calculated in two steps. The model of Parrot and Killoh [46] was first used to estimate the quantity of C_2S, C_3S, C_3A and C_4AF that had reacted after 28 days of hydration. Then, the volume fraction of each mineral (Table 3) was calculated with the geochemical module of HYTEC (CHESS). The initial total porosity was calculated from mineral and unhydrated clinker volume fraction of sound hydrated paste. The total porosity was 0.34 for the C_3A-rich sample and 0.40 for the C_3A-poor sample. The calculated porosities agree well with the porosity measured by autoradiography that were in the range of 0.35 to 0.40 for both pastes (Table 3). The initial pH of 13.5 was set by the Na^+ and K^+ hydroxide concentrations in the porewater.

As discussed in Sec. 2.1 (Fig. 1), the experimental profiles were obtained in a zone not affected by the initial crack generated in the sample. Only half 1-D configuration was required since the cylindrical samples were protected by resin laterally and the conditions were identical at both sides. In the cement paste, the grid was composed of 25 rectangular meshes in the first 0.1 cm, and 50 meshes from that point to 0.5 cm. The length of the tank solution zone of the grid was determined to keep the experimental ratio between the volume of solution (12×10^{-3} m^3 per sample) and the volume of the sample (7×10^{-6} m^3). Considering explicitly the tank in the reactive transport modeling was assumed to be more representative than simple Dirichlet boundary conditions [47]. The grid in the tank was more refined in the zone close to the boundary with the cement.

The D_e coefficient in the tank solution was equal to 10^{-9} m^2/s in a zone of 1 mm near the cement paste, and progressively increased to 10^{-5} m^2/s to simulate agitation of the solution. The initial chemistry of the solution was set to 30 mmol/L Na_2SO_4 and free to vary with time. Only the pH in the tank solution was constantly buffered to 7 by adding HNO_3. An initial effective diffusion coefficient D_e of 1×10^{-11} m^2/s was set to fit at best the whole set of experimental degradation fronts. This fitted D_e is within the range of values measured on CEM I hydrated pastes with a W/C ratio of 0.5 [48]. The same initial D_e was assumed for the C_3A-poor cement paste.

Table 3. Calculated total porosity from minerals and unhydrated clinker volume fractions and measured total porosity by autoradiography, for C_3A-rich and C_3A-poor cement pastes.

	C_3A-rich CEM I	C_3A-poor CEM I
Mineral vol. fraction		
Portlandite	0.14	0.15
C1.6SH	0.24	0.27
Ettringite	0.11	0.05
Monocarboaluminate	0.09	0.04
Unhydrated clinker volume fraction		
C_3A	0.008	0.003
C_3S	0.04	0.05
C_2S	0.02	0.03
C_4AF	0.01	0.01
Calculated total porosity (HYTEC)	0.34	0.40
Measured total porosity (autoradiography)	0.35 to 0.40 (uncertainty of 10%)	

2.4.4. Homogenization method

Macroscopic elastic properties were estimated from the reactive transport modeling results by the homogenization method of Mori-Tanaka [49]. Their scheme considers spherical inclusions embedded in an infinite matrix as well as interactions between inclusions. At the cement paste scale, the continuous reference matrix is the C-S-H matrix. The shear and compressibility coefficients of the equivalent homogenized material (k_{homo} and g_{homo}, respectively) are given by [49]:

$$k_{homo} = \frac{k_{C-S-H} + \frac{4g_{C-S-H}}{3}\sum_{i=1}^{N^{ph}} \varphi_i \frac{k_i - k_{C-S-H}}{k_i + \frac{4}{3}g_{C-S-}}}{1 - \sum_{i=1}^{N^{ph}} \varphi_i \frac{k_i - k_{C-S-H}}{k_i + \frac{4}{3}g_{C-S-H}}} \quad (3)$$

$$g_{homo} = \frac{g_{C-S-H} + H_{C-S-H} \sum_{i=1}^{N^{ph}} \varphi_i \frac{g_i - g_{C-S-H}}{g_i + H_{C-S-H}}}{1 - \sum_{i=1}^{N^{ph}} \varphi_i \frac{g_i - g_{C-S-H}}{g_i + H_{C-S-H}}} \quad (4)$$

where N^{ph} is the number of phases, k_{C-S-H} and g_{C-S-H} the shear and compressibility coefficients of C-S-H, k_i and g_i the shear and compressibility coefficients of the phase i, φ_i the volume fraction of the phase i and H_{C-S-H} is the following term [49]:

$$H_{C-S-H} = \frac{g_{C-S-H}(\frac{3}{2}k_{C-S-H} + \frac{4}{3}g_{C-S-H})}{(k_{C-S-H} + 2g_{C-S-H})} \quad (5)$$

3. Results

3.1. Mineralogical evolution over time

3.1.1. Phase distribution in the degraded zone

XRD analyses were made on the C_3A-poor samples after 2 months, 4 months and 6 months of degradation. Acquisition of XRD patterns of C_3A-rich cement pastes was only achievable after 2 months and 4 months, since the 6-month degraded sample was heavily damaged. The X-ray diffraction angles for characterizing the mineralogy corresponded to the main peak of ettringite (3.85 Å), gypsum (4.65 Å), portlandite (2.62 Å) and monocarboaluminates (7.18 Å). Hydration products such as portlandite, C-S-H, ettringite, monocarboaluminate and hemicarboaluminate were identified in both sound cement pastes as well as anhydrous cement phases such as C_4AF. AFm phase peaks were highly detectable for the C_3A-rich cement paste in contrast to the C_3A-poor sample. In the latter, few aluminate phases were formed during hydration due to the low amount of aluminum and were, therefore, difficult to detect.

Mineral peak heights (Fig. 3) were plotted as a function of depth. The peak of C_4AF that usually hydrates very slowly and is present at a relatively constant amount over time was hardly identified in the present XRD diagrams. Therefore, for visualization purposes only, normalization was performed to the portlandite peak in the sound zone due its ease of identification and high intensity. The mineralogical composition in the degraded zone was common to all samples. From the attacked surface to the center, a first zone was found in which ettringite was the main detected mineral. Further down, the precipitation of both gypsum and ettringite was revealed and, the coexistence of ettringite, portlandite and gypsum was also identified before reaching the sound part. This mineralogical distribution is in line with the experimental results of [10,50,51]. The gypsum precipitation front showed a progressive widening over time while migrating towards the interior of the sample. The layer thickness of gypsum formation was greater for the C_3A-poor cement paste, approximatively 600 µm at 2 months and 800 µm at 6 months, compared to 400 µm and 700 µm for the C_3A-rich sample, respectively. Secondary ettringite precipitation occurred in the leached zone. The XRD peaks' intensity of ettringite was much higher in the leached zone than in the sound zone, suggesting the formation of new crystals corresponding to secondary ettringite. The intensity of the related peaks increased from the sample center to the outer zone, and then sharply decreased near the surface. The limit of the degraded zone was assumed to correspond to the depth at which monocarboaluminate was detected. In the case of the C_3A-poor sample, detection of

monocarboaluminate was proven ambiguous and could be confused with background noise due to very low peaks. For the sake of clarity, monocarboaluminate detection depth was not shown for the C_3A-poor sample. XRD patterns of the C_3A-rich pastes showed that gypsum was not detected in the zone where monocarboaluminate was still present, which suggested a gap between the front of ettringite precipitation from monocarboaluminate and the front of gypsum precipitation.

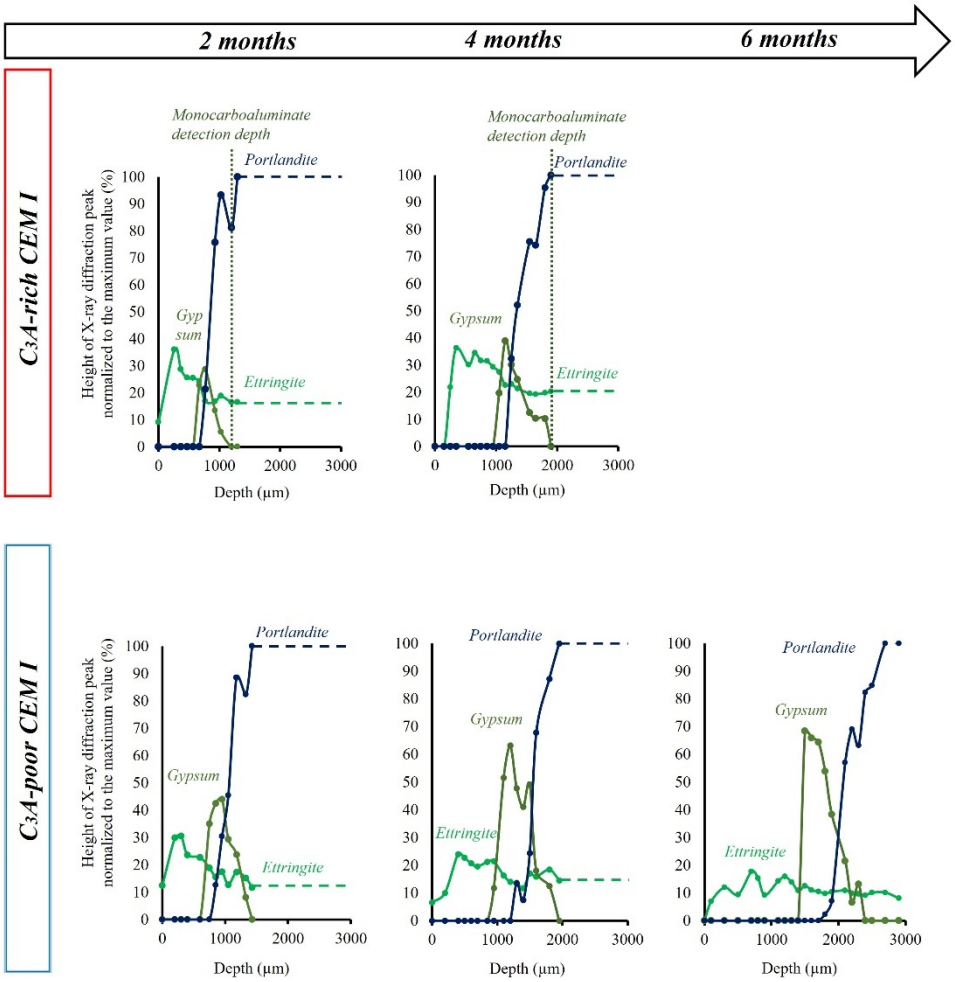

Fig. 3. Evolution over time of the relative XRD intensity profiles of portlandite (2.62 Å), ettringite (3.85 Å) and gypsum (4.65 Å), as well as depth from which the monocarboaluminate (7.18 Å) was detected.

3.1.2. Cement paste decalcification

The decalcified zone was also identified by using the SEM-EDS results. The limits of decalcification (Table 4) corresponded to the depth from which the Ca intensity signal starts decreasing from the base value at the center of the sample. These limits were consistent with the portlandite dissolution depths obtained by XRD (Fig. 3). The progression of the decalcification depths with time was very close for both cement pastes. But after 6 months, the decalcification depth of the C_3A-rich cement was more than 1000 µm higher.

Table 4. Progression with time of the experimental and calculated depths of portlandite depletion.

	Exp. decalcification limit (SEM-EDS)	Exp. portlandite depletion depth (XRD)	Calcul. portlandite depletion depth (HYTEC)
C_3A-rich CEM I			
15 days	500 µm	-	500 µm
2 months	1000	800	950
4 months	1400	1200	1400
6 months	3000	-	1700
C_3A-poor CEM I			
15 days	500 µm	-	500 µm
2 months	800	800	900
4 months	1500	1300	1300
6 months	2100	1800	1700

3.2. Microstructural evolution in the calcium depleted zone

3.2.1 SEM-EDS analysis

A particular focus was given to the samples degraded for 6 months. SEM-EDS acquisition was performed on the whole thickness of the cement paste to characterize both degraded sides of the samples. Fig. 4 shows the elementary maps of calcium and sulfur. Ca elementary maps of both samples highlighted the Ca-depleted zone, by showing several levels of decalcification as the Ca signal intensity gradually decreased from the center of the sample to the exposed surface. S elementary maps revealed low sulfur concentration in the most decalcified zone, near the attacked surface. A section highly enriched in S was identified at approximatively 1800 µm from the attacked surface, which ended at the boundary of the Ca-depleted zone for both cement pastes. According to XRD results carried out on the C_3A-poor cement paste (Fig. 3), this section in which the S signal is the highest corresponds to the precipitation of gypsum and ends near the portlandite dissolution front. Analyses performed on both sides of samples highlighted a symmetry of degradation in the direction of diffusion. A significant difference between the two samples was the existence of straight-line sections parallel to the attacked surface which were deprived in Ca and S for the C_3A-rich cement paste. These sections were located at the interface between the sound and degraded zones, as well as at 1800 µm near the limit of the S-enriched zone.

3.2.2 Microtomography

Microtomography displayed macroporosity opening in the Ca-depleted zones for the C_3A-rich (Fig. 5a) and C_3A-poor samples (Fig. 5b), respectively. Relative average density was extracted and compared to Ca/Fe and S/Fe intensity ratios obtained from SEM-EDS analyses (Fig. 5c). In fact, the Ca signal intensity was normalized with the Fe signal intensity as Fe is expected to remain relatively stable throughout the degradation process. For both pastes, a simultaneous linear decreasing of the Ca intensity and the relative average density was observed from the sound core (around 3000 µm) to the surface in contact with the solution. A slight increase in density was revealed for the C_3A-rich paste at approximatively 2200 µm where the S intensity was the highest. This phenomenon was also observed for the C_3A-poor sample, although a

decrease of the density curve steepness was noticed instead. Furthermore, a considerable decrease of Ca intensity was observed in the C_3A-rich cement paste from 2700 µm from the external surface to 3000 µm after the increase of the S intensity ratio. SEM-EDS acquisition showed that this drop in Ca intensity was attributed to the localization of cracks (Fig. 5).

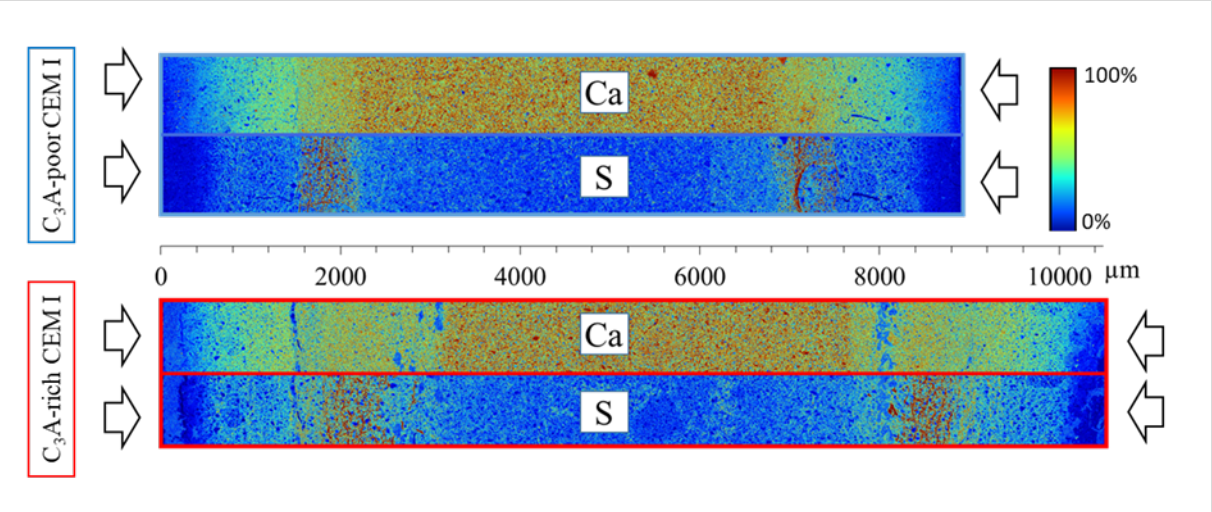

Fig. 4. EDS elementary map of Ca and S. Elementary map scale provides the percentage of the element in each pixel, from 0% in blue to 100% in red. Diffusion of the Na_2SO_4 solution is indicated by arrows.

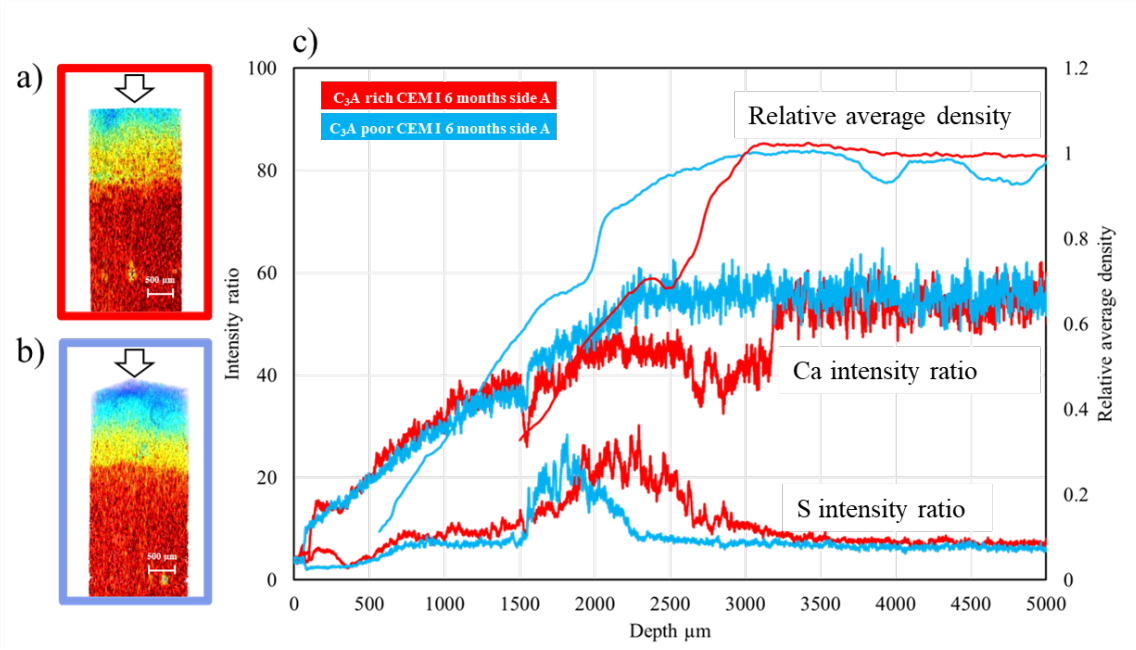

Fig. 5. Computed images obtained by microtomography of the C_3A rich CEM I paste (a) and the C_3A poor CEM I paste (b) after 6 months of degradation showing macroporosity opening. The right graph (c) displays the superposition of the relative average density built from the microtomography data and the Ca/Fe and S/Fe intensity ratios built from the EDS maps.

3.3. Reactive transport modeling

3.3.1 Modelling of the successive mineralogical fronts

The density of ettringite had to be adjusted in order to better model the depths of the chemical degradation fronts. The density was increased from 1767 kg/m^3 to 2500 kg/m^3 (Table 2). This adjustment has no physical meaning by itself but used to correct some artefacts of the modeling. In particular, a transient peak of ettringite precipitation was calculated on the right-hand side of the zone where ettringite fully dissolved (Fig. 6). This peak led to a transient sharp decrease of porosity and De. From a more physical point of view, a single porosity was considered in the present HYTEC modeling without any homogenization procedure of different types of porosity (e.g. intra C-S-H and capillary ones). In reality, porosity clogging could have been distributed between different types of porosity (e.g. capillary porosity vs. intra C-S-H porosity) keeping diffusion pathways more open as modeled with an unique porosity. Reducing the density (or equivalently reducing the molar volume) attenuated the clogging by ettringite formation through the Archie law (Eq. 2). Ettringite formation in pores could also have induced localized microcracks that would have locally enhanced diffusion. Such an effect could not be considered in HYTEC modeling.

Figs. 6 and 7 indicate three successive dissolution fronts in the reactive transport modeling of both types of cement. The first front stands in the zone further away from the exposed surface, where SO_4^{2-} diffusion leads to ettringite precipitation at the expense of the dissolution of monocarboaluminate and a small fraction of portlandite. The second front occurs closer to the exposed surface, which corresponds to a band of gypsum formation associated with massive portlandite dissolution. The gypsum band shifts with time, as highlighted by the comparison of the modeling results after 4 and 6 months of degradation. In contrast, the secondary ettringite does not redissolve, except near the exposed surface, which constitutes a third front showing a complete dissolution of the cement hydrates over 200 µm from the attacked surface. The simulations of Figs. 6 and 7 indicate portlandite dissolution followed by a progressive decalcification of C-S-H with the Ca/Si ratio decreasing from 1.6 to 0.8. Such a hydrolysis mechanism was in good agreement with the measured decrease of the Ca intensity ratio from the core of the material to the outermost zone. The experimental data indicated a clear decrease of Ca and S the boundary of the chemically degraded cement pastes, but not a full depletion.

Not shown here, SEM-EDS analysis pointed out the occurrence of a Si-Al gel that could not be modeled due to the lack of thermodynamic data. Accordingly, amorphous SiO_2 and micro-crystalline Al hydroxide AH3(mc) were considered as pure separated poles to model this most advanced state of the cement leaching. But these two solid phases never precipitated in the present HYTEC modeling. Micro-crystalline and amorphous AH3 have been observed in cementitious system at 20 °C [52], whereas gibbsite forms generally at higher temperatures due to kinetic hindrance. Gibbsite was also tested as an alternative to AH3(mc) since it is thermodynamically more stable, but it did not precipitate in the modelling too. Nevertheless, the disagreement between the model and the experiment with respect to the gel formation only occurred at the very first hundreds of microns and did not really affect the global modeling of the sulfate attack.

After 4 months of degradation (Fig. 6), the portlandite dissolution depths calculated with HYTEC agreed very well with the experimental results (Table 4). The calculated depths of gypsum precipitation were also in good agreement with experimental data (Fig. 3). The gypsum front was located where the experimental S-enriched zone was detected, i.e. right before the portlandite dissolution front. The calculated thickness of the gypsum band was also in line with measurements, although slightly underestimated in the C_3A-poor cement paste. As expected,

the HYTEC simulations led to a lower amount of ettringite and a higher quantity of gypsum in the C_3A-poor sample than in the C_3A-rich one. In fact, the sulfate ingress from the reservoir into the material maintained the formation of gypsum while the removal of Ca^{2+} by diffusion from the material in the reservoir caused its dissolution. Gypsum stored SO_4^{2-} as it was formed, which was available sooner in the C_3A-poor cement paste, leading to a larger formation of gypsum (Figs. 6 and 7).

SEM-EDS showed that the experimental thickness of the S-enriched zone was larger and the signal slightly higher for the C_3A-poor sample. But SEM-EDS did not allow to differentiate gypsum from ettringite, as well as small ettringite crystals from the C-S-H matrix in which they were mixed. Nonetheless, XRD analyses (Fig. 3) certainly indicated a higher proportion of gypsum than ettringite in the C_3A-poor paste. The comparison of Fig. 3 (XRD) and Fig. 6 (modeling) reveals a discrepancy between modeling and experiment. The modeling led to a more significant decoupling between the monocarboaluminate/ettringite front and the gypsum formation front. This point already found in other modeling studies from the literature will be further discussed in Sec. 4.1.

After 6 months of degradation (Fig. 7), the simulation results were globally in line with experimental data concerning portlandite dissolution (Table 4), the decalcification zone and gypsum formation depth in the C_3A-poor paste. On the contrary, the model failed to simulate the experimental data for the C_3A-rich paste. The depth of portlandite dissolution, the thickness of the gypsum band and the Ca-depleted zone were underestimated significantly. The model did not take into account the cracks that in reality had surely enhanced SO_4^{2-} diffusion and probably also gypsum re-dissolution.

The calculated profiles of mineral volume plotted as a function of depth in Figs. 6 and 7 highlight the impact of phase precipitation on transport properties (diffusion coefficient and porosity). First, the porosity slightly decreases as soon as ettringite precipitates, despite the dissolution of monocarboaluminate. This illustrates the clogging action of ettringite due to its large molar volume, even though the molar volume of the database was reduced. Inversely, portlandite total dissolution causes a rise in porosity. A localized decrease of porosity is then found at the gypsum peak for both pastes but more pronounced in the C_3A-poor one. Porosity moderately rises with C-S-H decalcification stages, to reach approximatively 0.9 in the Si-Al gel zone very near to the exposed surface. The unhydrated clinker stands for the remaining volume fraction, i.e. porosity did not reach one in the model despite the full dissolution of the hydrates. The strong increase of porosity in the leached zones agrees well with the microtomography data of Fig. 5.

3.3.2. Modeling of the pore water and tank chemistry

Regarding the modeling of the porewater chemistry inside the cement paste (Fig. 6), the Ca^{2+} total concentration increased after the first portlandite dissolution front, then reached its maximum value at the portlandite complete dissolution front and eventually decreased to zero at the boundary conditions. Sulfates diffused from the leaching solution into the sound core to be integrated into gypsum and secondary ettringite. The calculated pH quickly decreased from 13.5 to 12.75 due to Na-K-OH diffusion. The pH was then buffered around 12.75 in the zone of monocarboaluminate/ettringite transformation, and progressively decreased within the decalcified zone in the direction of the boundary conditions.

The chemistry of the tank solution (not shown) was only slightly modified by the hydrate dissolution due to its large volume, both in the modeling and the experiment. In the modeling, the SO_4 total concentration changed from 30 mmol/L to 29 mmol/L after 6 months. The

strongest evolution was calculated for the Ca^{2+} total concentration from 0 to 1 mmol/L due to the leaching of the Ca-hydrated phases. The Na^{+} concentration remained constant at 60 mmol/L, and the concentration of K^{+} was 0.1 mmol/L. The pH remained fixed to 7 during all the duration. Experimentally, the concentration of Ca^{2+}, SO_4^{2-}, Na^{+} and K^{+} measured in the solution after 6 months were respectively of 1.2, 28.5, 62 and 0.06 mmol/L with an uncertainty varying between 2 and 6% depending on the ion measured.

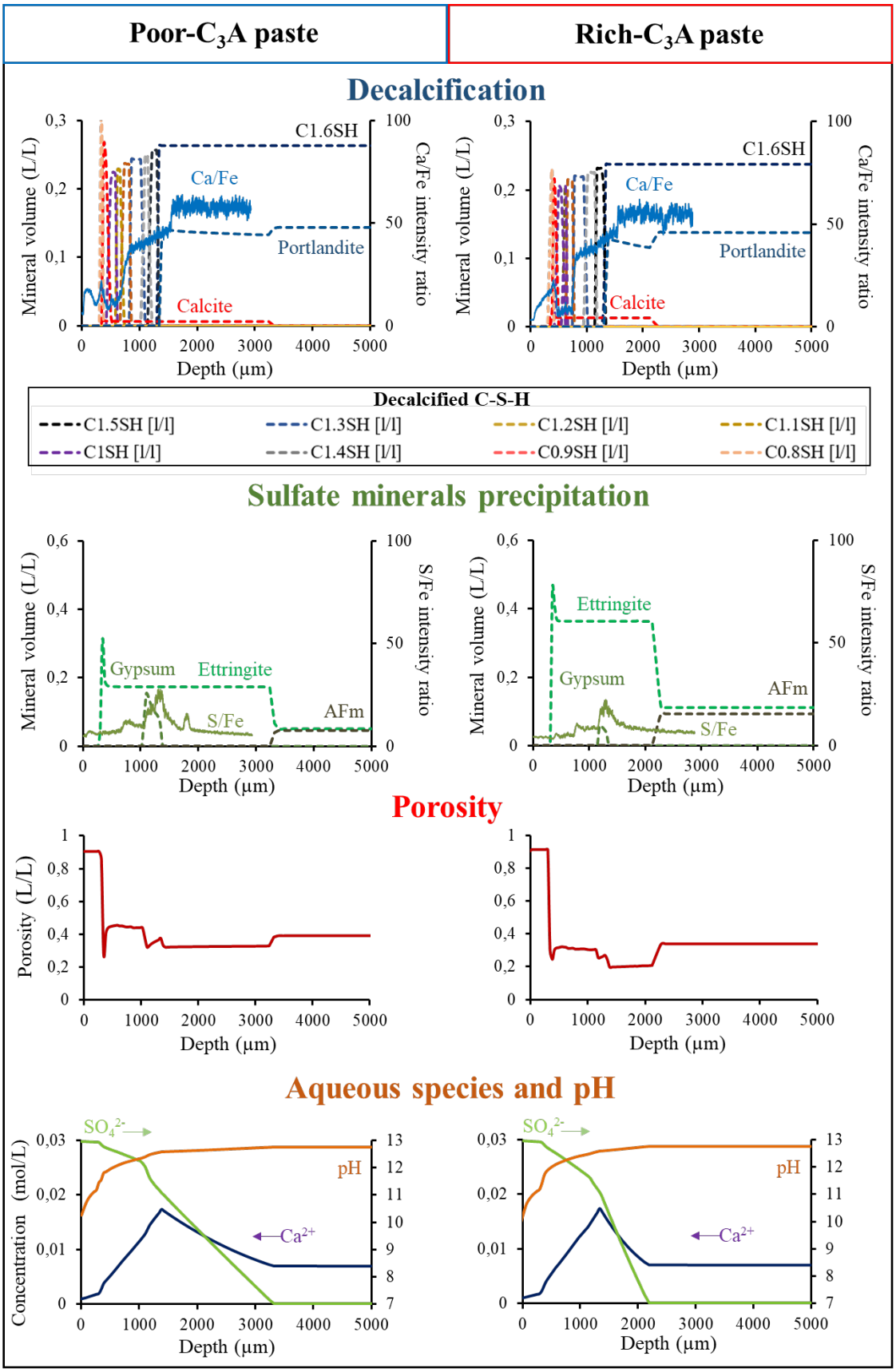

Fig. 6. HYTEC modeling at 4 months showing profiles of mineral (volume fraction), total porosity, pH, Ca^{2+} and SO_4^{2-} total concentrations. The experimental intensity ratios of Ca/Fe and S/Fe (EDS) are given for comparison.

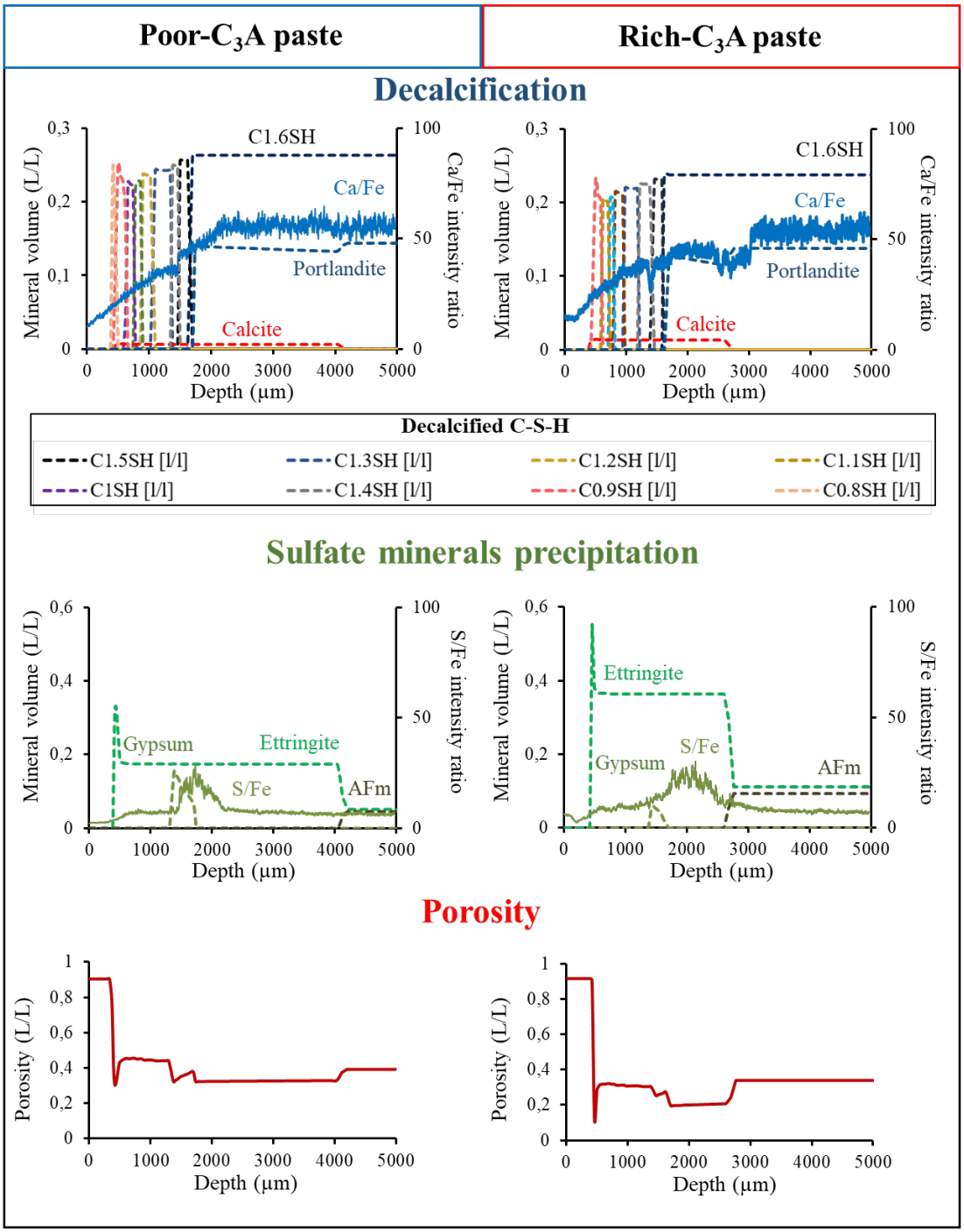

Fig. 7. HYTEC modeling at 6 months showing profiles of mineral (volume fraction), total porosity, pH, Ca^{2+} and SO_4^{2-} total concentrations. The experimental intensity ratios of Ca/Fe and S/Fe (EDS) are given for comparison.

3.4. Evolution of mechanical properties

3.4.1. Nanoindentation measurement and homogenization method

A discrete distribution map of Young's modulus was performed by microindentation on each sample going from one exposed surface to the other one (Fig. 8a). The Young's modulus decreased from the center of the paste to the attacked surface over a depth of 2000 µm and 3000 µm for the C_3A-poor and C_3A-rich samples, respectively. The measured value in the sound

zone was approximatively 20 GPa and decreased to less than 5 GPa in the outermost zone. In order to compare the evolution of mechanical and chemical properties, microindentation measurements were plotted with the Ca and S intensity ratios extracted from SEM-EDS (Fig. 8b). A slight dispersion of the measured values was observed at the same depth since cement pastes are heterogeneous materials. This may be due to the simultaneous presence of more than one phase in the indented zone because of the macro-scale at which indentation proceeded. Average properties were calculated at each measured depth after removing values greater than 40 GPa attributed to the only presence of anhydrous phases such as C_3S, C_2S, C_3A, C_4AF which have a Young's modulus of 117.6 GPa [45].

The modulus of elasticity measured as a function of depth in the C_3A-poor sample indicated a linear decrease in the leached zone, from 20 to 5 GPa. Similarly, the measured Young's moduli decreased as the intensity ratio of Ca dropped, which suggests a loss of mechanical properties due to decalcification. Regarding the C_3A-rich cement paste, a similar decrease of Young's moduli from 20 GPa to less than 5 GPa near the exposed surface was also observed and well correlated to the reduction of the Ca intensity ratio. However, this decrease was not linear as with the C_3A-poor sample. A first sharp drop was measured at 3000 µm from the exposed surface, the Young's modulus going from 20 GPa in the sound zone to less than 15 GPa before reaching 20 GPa again. A linear decrease to a value lower than 5 GPa took place in the most leached zones. Comparison with the Ca intensity ratio indicated that these drops occurred at the level of the observed cracks and resulted from microcracking in the zone near the main cracks. The superposition of these results with the intensity ratio of sulfur shows that such drops (as well as the material discontinuities) were localized on both sides of the gypsum band. The precipitation of sulfate minerals indicated by the increase of the S intensity ratio in Fig. 8 did not suggest any impact on the measured Young's modulus, even in the zone of gypsum precipitation.

The micro-mechanical properties were then calculated from the Mori-Tanaka homogenization scheme (Sec. 2.4.3) based on the HYTEC modeling results. One considered a cement paste whose matrix was composed of C-S-H of different Ca/Si ratio and inclusions randomly distributed in orientation and space. The inclusions in the scheme were hydrates, capillary porosity and anhydrous cement. The total porosity ϕ given in HYTEC includes two families of pores, gel pores and capillary pores, respectively noted ϕ_{C-S-H} and ϕ_{cap} in the following equation:

$$\phi = \phi_{C-S-H} + \phi_{cap} \quad (6)$$

Based on Tennis and Jenning work, gel porosity was estimated from the C-S-H volume fraction [53]:

$$\phi_{C-S-H} = \alpha_{C-S-H}\ \varphi_{C-S-H} \quad (7)$$

where α_{C-S-H} is a coefficient equal to 0.28 [53] and φ_i the volume fraction of phase i.

At the cement paste scale, the following equation has to be satisfied [54]:

$$1 = \phi_{cap} + \sum_{i}^{Nph} \varphi_i \tag{8}$$

where Nph is the number of phases.

C-S-H volume fraction and capillary porosity were estimated from the previous equations and given by Eqs. 9 and 10, respectively [54]:

$$\phi_{cap} = \frac{\phi - \alpha_{C-S-H}\,(1 - \sum_{i}^{Nph-1} \varphi_i)}{1 - \alpha_{C-S-H}} \tag{9}$$

$$\varphi_{C-S-H} = \frac{(1 - \sum_{i}^{Nph-1} \varphi_i) - \phi}{1 - \alpha_{C-S-H}} \tag{10}$$

The homogenization method relied on the volume fractions of each mineral phase provided by the previous chemical degradation simulations and the mechanical properties of Table 2. The mechanical properties of C-S-H were determined from the Constantinides and Ulm work [55]. They estimated the elastic modulus of sound and degraded C-S-H as 23.8 and 4.3 GPa, respectively. Subsequently, these values were used to determine the decalcified C-S-H Young's modulus E_{CSH} evolution as a function of the Ca/Si ratio based on the following equation [56]:

$$\begin{cases} if \quad \dfrac{C}{S} > 0.8, & E_{CSH} = \left(1 - \dfrac{C/S - 0.8}{1.65 - 0.8}\right) E_{CSH}^{UL} + \dfrac{C/S - 0.8}{1.65 - 0.8} E_{CSH}^{S} \\ if \quad \dfrac{C}{S} \leq 0.8, & E_{CSH} = E_{CSH}^{UL} \end{cases} \tag{11}$$

where E_{CSH}^{UL} and E_{CSH}^{S} are the Young's modulus of uniformly leached and sound C-S-H, respectively. Poisson ratio values were assumed to be unaffected by calcium leaching [55].

In the most leached zone, located from 200 µm from the exposed surface, the complete dissolution of the cement hydrates occurred (Fig. 7). In the homogenization calculations, it was assumed that the anhydrous phases were dissolved as well, and that only a silica gel remained which had the same mechanical properties as the C-S-H with a Ca/Si ratio lower than 0.8. Its volume fraction was 0.1 and was calculated based on the silica content of the cement paste and on the density of amorphous silica [44]. Moreover, the real density of ettringite was considered during the homogenization calculations (1767 kg/m^3 [44]).

Fig. 8c shows that a slight decrease of the Young's modulus was calculated for both C_3A-rich and C_3A-poor cement pastes at the monocarboaluminate and ettringite transformation front, linked to the partial dissolution of portlandite. A more significant decrease occurred at the total dissolution front of the portlandite. This reduction took place in several stages corresponding to the various C-S-H decalcification fronts. In the most decalcified zone where ettringite was completely dissolved and only amorphous gel remained, the calculated Young's modulus

reached a final value of 5 GPa for both cement pastes in good agreement with the experimental results.

Nevertheless, differences were calculated between the two types of cement pastes. The Young's modulus quickly reached values lower than 10 GPa in the C_3A-rich paste after a decrease linked to the total dissolution of portlandite, while in the C_3A-poor paste Young's modulus varied between 15 GPa and slightly below 10 GPa over the whole zone not entirely decalcified. These two modeling results were in good agreement with the experimental ones, since the mechanical properties measured in the C_3A-rich paste at the level of the non-cracked zones were also higher than in the C_3A-poor paste. However, the rapid decrease in mechanical properties measured experimentally due to the presence of cracks could not be represented in the homogenization results, since cracking was not taken into account in the reactive transport modeling and the micromechanical model.

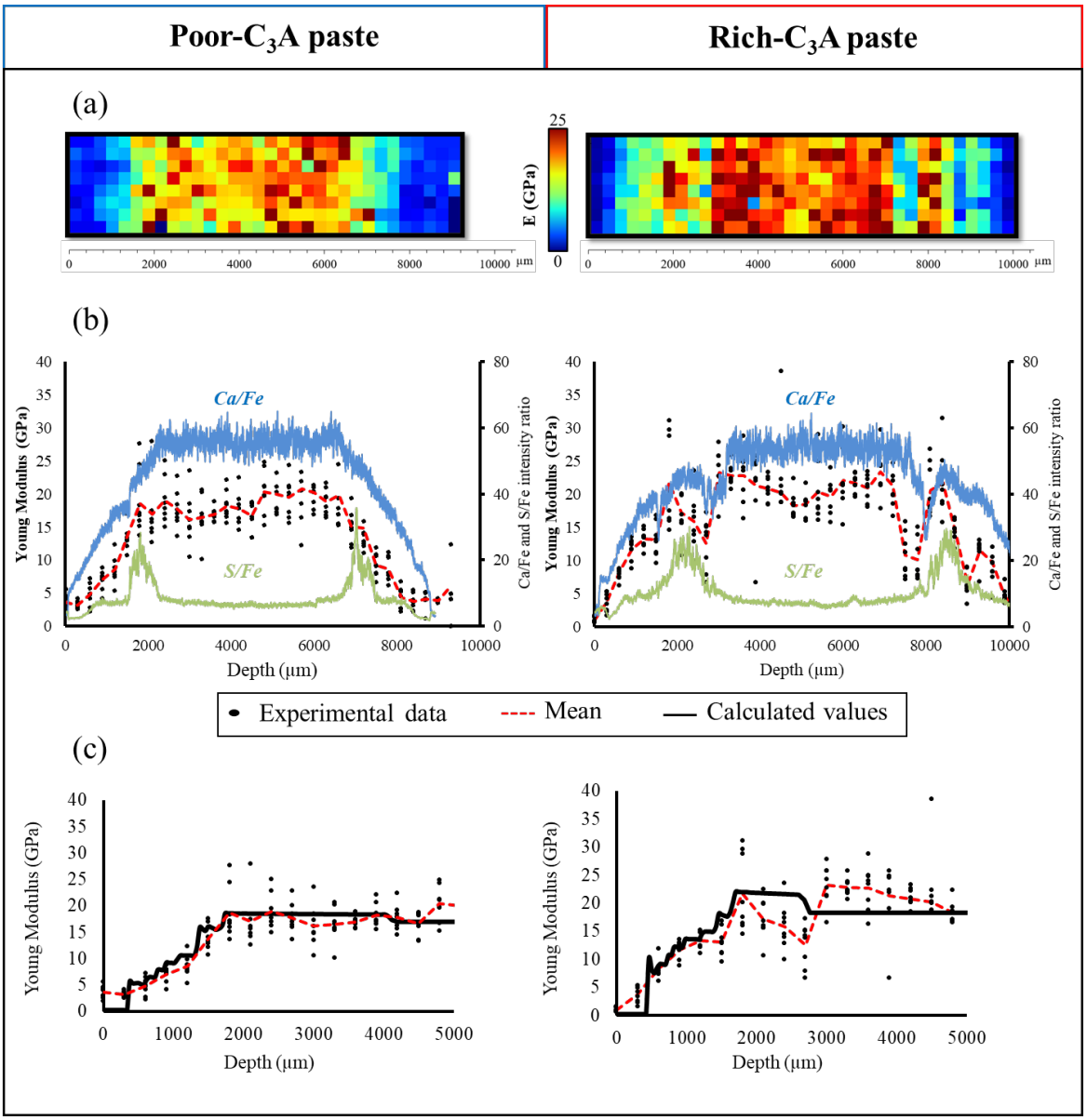

Fig. 8. (a) Mapping of Young's modulus in the cement paste. (b) Evolution of Young's modulus with depth obtained by nanoindentation combined with Ca/Fe and S/Fe intensity ratios. (c) Comparison of elastic properties between homogenized values and experimental results.

3.4.2. Correlation between cracking and mineralogy

The location of gypsum was identified from the Ca and S elementary maps by using the reference spectrum of Fig. 2. Cracking profiles were extracted from the SEM-EDS acquisition and their location were indicated on the maps (Fig. 9). These results are shown for the C_3A-poor and C_3A-rich samples after 2 months, 4 months and 6 months. For samples degraded for 6 months, both sides of the samples were analyzed, noted side A and side B. Gypsum precipitation had the shape of a band that widened and moved with time, in consistency with the XRD results. The C_3A-rich cement pastes showed cracks parallel to the attacked surface located on both sides of the gypsum band after 4 and 6 months of degradation. After 4 months, the crack presented an opening of about 50 µm, while after 6 months, the thickness of the crack located before the sound zone was about 300 µm. Cracks formed before gypsum precipitation area were also observed for the C_3A-poor cement paste after 6 months (some cracks related to artefacts were observed but not represented in Fig. 9).

A focus was made on the cracking obtained at 6 months in the C_3A-rich cement paste. A small section of the paste was analyzed by microtomography directly after its removal from the solution, without being vacuum packed, embedded, or polished, to avoid formation of cracks related to the preparation of the sample. Fig. 10 displays these results in which a progressive opening of porosity was noted from the attacked surface to the center of the specimen. This opening of porosity took place on approximately 3000 µm and corresponded to the decalcified depth, as shown by the elementary maps of Fig. 5. A significant observation was the presence of a straight zone located between 2700 and 3000 µm, in which the density was very low. The comparison with elementary maps (Fig. 4) showed that the location of cracks corresponds to a depletion of Ca and S. A part of the degraded zone was separated from the rest of the material due to its brittle nature, induced by a very significant damage. Fig. 10b shows the zones in which the density was the lowest, as well as the two plans of cracking parallel to the attacked surface. These two cracks are located at the same position in the degraded zone, i.e. right before reaching the sound zone. Some macropores were also observed in the sound zone. These cracks took the form of a plan parallel to the exposed surface and had the same thickness on both sides, which was about 300 µm. Microtomography analyses of these cracks on both side of the sample confirmed that they were caused by the external sulfate attack and not by any artefacts of sample preparation. On the contrary, the cracks located before the gypsum band were probably related to the sample preparation since noticeable only from SEM-EDS acquisition (Fig. 9.).

Fig. 11 shows the results of the C_3A-poor sample degraded during 8 months. The gypsum formation band occurred from 1.5 mm to 2 mm. Fig. 11 also indicates the relics of the cracks that could be induced by previous gypsum precipitation from 1 mm to 1.5 mm. Such vertical cracks had shapes and dimensions similar to the gypsum veins observed after 6 months. Moreover, additional localized micro-cracks were detected in the gypsum band near the limit of the decalcified zone. These micro-cracks appear to have originated from localized zones and their widths typically range between 1 to 3 micrometers.

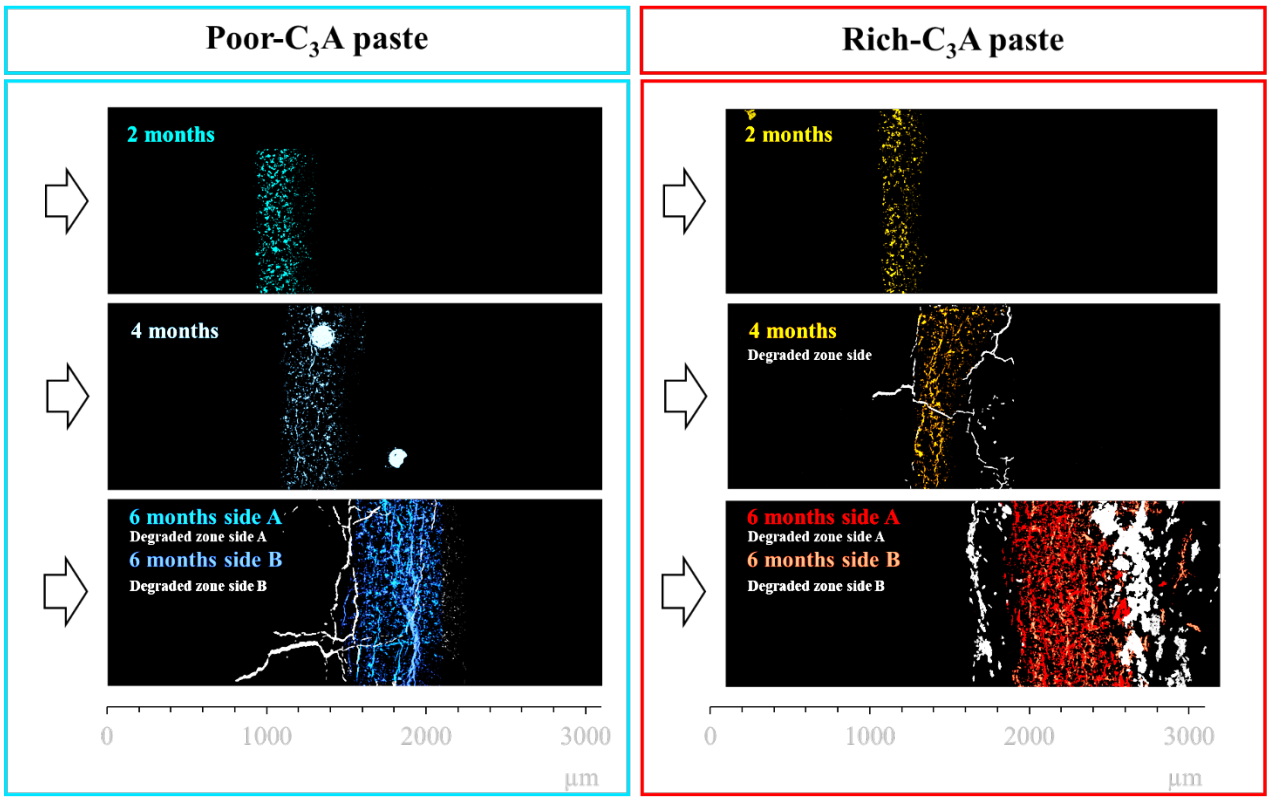

Fig. 9. Evolution of gypsum precipitation and cracking over time.

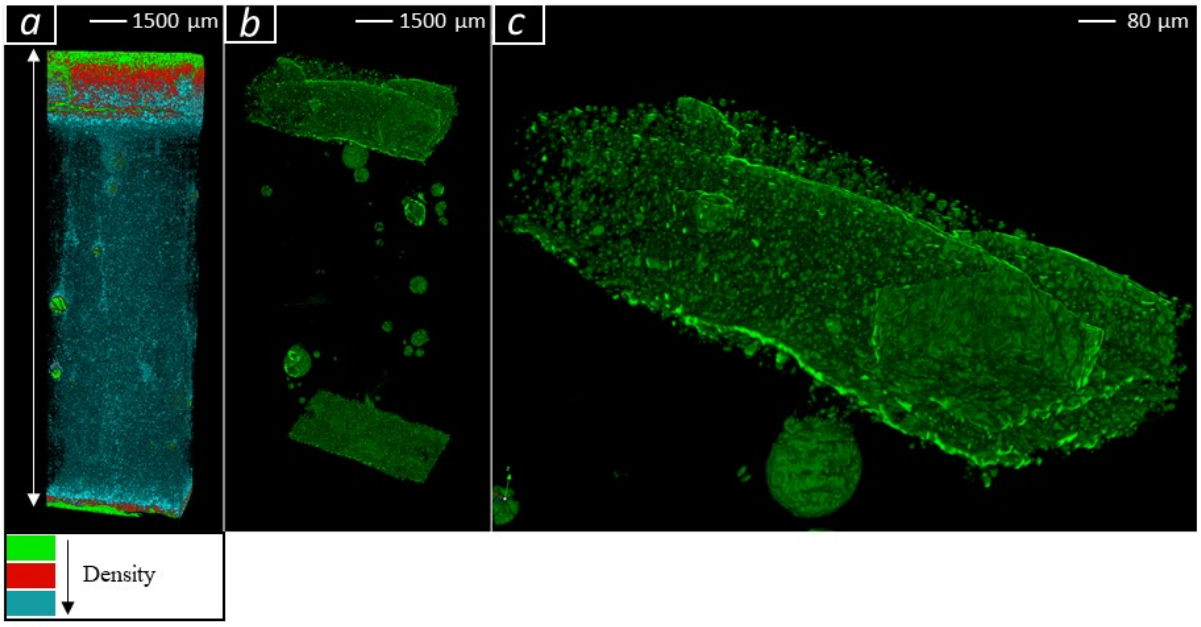

Fig. 10. (a) Reconstruction of macroporosity and cracking in the C_3A-rich paste from microtomography analyses after 6 months of degradation; (b) extraction of sections of lowest density; (c) zoom on the top cracked section.

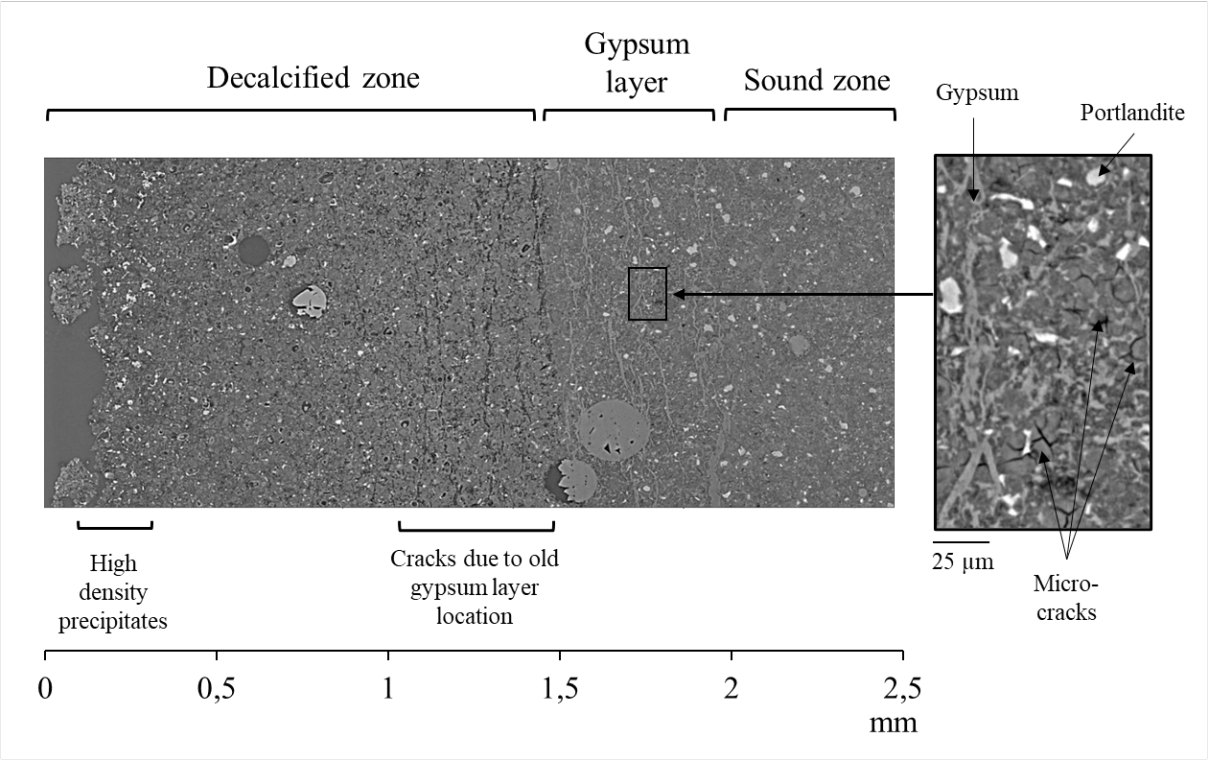

Fig. 11. Microtomography scan of the C_3A-poor paste after 8 months of degradation; the exposed surface is on the left-hand side.

4. Discussion

4.1. *Competition between hydrolysis, ettringite precipitation and gypsum precipitation*

The Na_2SO_4 solution did not only induce a moderate external sulfate attack (ESA) but also hydrolysis process since the neutral pH and the null content in Ca were aggressive for the Ca-hydrated cement phases. Fig. 12a gives complementary HYTEC modeling results in which the leaching solution consisted of pure water at a fixed pH of 7. The main difference with the Na_2SO_4 attack is that the formation of ettringite is lower in terms of mass (or volume) and that there is no transformation of monocarboaluminate into ettringite (only a dissolution of these two Al-cement phases). On the contrary, the front of portlandite dissolution progresses rather similarly without any chemical coupling with the monocarbonate/ettringite front in both solutions (the precipitation of ettringite had a physical effect in the Na_2SO_4 case by reducing the porosity and diffusive transfer). The dissolution of ettringite at the boundary and of portlandite inside the cement is mainly triggered by the hydrolysis.

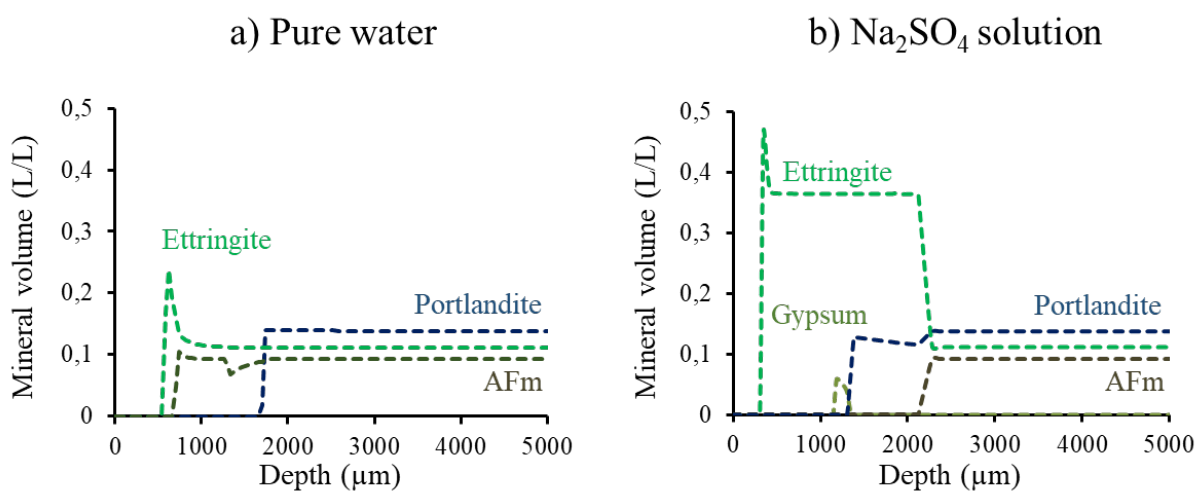

Fig. 12. HYTEC modeling comparing the degradation fronts at 4 months due to an attack of the C_3A-rich cement paste by (a) a solution of pure water at pH 7 (hydrolysis) and (b) a solution of Na_2SO_4 30×10^{-3} mol/L at pH 7 (hydrolysis and moderate ESA).

In addition to hydrolysis, diffusion of SO_4^{2-} ions in the interstitial solution induced a series of chemical reactions in the cement paste. A first stage of reaction is the transformation of monocarboaluminate to ettringite under the condition that Ca^{2+} are provided by a partial dissolution of portlandite:

$$3CaO.Al_2O_3.CaCO_3.11H_2O + 3Ca(OH)_2 + 3Na_2SO_4 + 21H_2O \rightarrow 3CaO.Al_2O_3.3CaSO_4.32H_2O + 6NaOH + CaCO_3 \quad (12)$$

According to the HYTEC calculations, Eq. 12 kept SO_4^{2-} at a low total aqueous concentration in contrast with a relatively high Ca^{2+} total concentration. The modeling led to a pH slightly above the portlandite buffer by 0.15 pH unit due to the release of OH^- (expressed as NaOH in Eq. 12). The modeling predicted the precipitation of calcite, whereas XRD analysis did not point out any occurrence of $CaCO_3$ polymorphs (aragonite, calcite, vaterite) in the samples. It is not clear whether this lack of $CaCO_3$ was due to a high detection limit in XRD or to a kinetic inhibition. Calcite was not taken into account in the calculations of the elastic properties.

In a second stage of reactions, the full dissolution of portlandite (hydrolysis front, Eq. 13) provides Ca^{2+} ions that lead to formation of gypsum in the presence of sulfates (Eq. 14):

$$Ca(OH)_2 \rightarrow Ca^{2+} + 2OH^- \quad (13)$$

$$Ca^{2+} + Na_2SO_4 + 2H_2O \rightarrow CaSO_4.2H_2O + 2Na^+ \quad (14)$$

Under the present weak concentration in Na_2SO_4, the driving force is the hydrolysis reaction and not the formation of gypsum. The formation of gypsum occurs as a by-product of hydrolysis.

The local increase in porosity due to portlandite dissolution facilitated the upstream diffusion of SO_4^{2-}. According to Damidot and Glasser [57], for the system of CaO-Al_2O_3 -$CaSO_4$ -H_2O at 25°C, the portlandite/gypsum invariant point corresponds to a SO_4^{2-} total concentration of 11.5 mmol/L. Modeling results showed that this possible threshold of gypsum precipitation in presence of portlandite was reached only in a zone where the accumulation of sulfate in solution was large enough, far from the monocarboaluminate/ettringite transformation front that

consumed sulfate. Once the aluminum provided by AFm phase dissolution is depleted, ettringite formation ends, and SO_4^{2-} reacts with portlandite to form gypsum [4,7,50].

A key parameter is, therefore, the initial amount of AFm phases, either as hemicarboaluminate, monocarboaluminate or monosulfoaluminate. In the C_3A-rich cement paste, more Al was provided by the monocarboaluminate to precipitate ettringite which lowered gypsum precipitation over a given duration. In the C_3A-poor cement paste, a larger amount of gypsum was formed due to reduced ettringite precipitation. For both cement types, HYTEC modeling indicated the conservation between the moles of Al in monocarboaluminate, the only primary source of Al in the model, and the moles of Al in neoformed ettringite. XRD analysis of cement pastes degraded during 2 months and 4 months showed a wider thickness of gypsum band in the C_3A-poor cement paste compared to the C_3A-rich one, and the SEM-EDS S intensity corresponding to gypsum precipitation was greater for the C_3A-poor sample. To come back to the issue of the coupling between hydrolysis and ESA, a main difference between the thermodynamic titration exercises and the present reactive transport modeling is that the dissolution of portlandite is not driven by the increase in SO_4 concentration to form gypsum, but by the hydrolysis process induced by the tank solution at pH 7.

In the present experiments, the different analysis such as XRD clearly indicated that gypsum precipitation occurred near the portlandite dissolution front. The analysis indicated a shift between the maximum of gypsum precipitation and of the front of ettringite formation for the C_3A-rich cement, but much lower than in the modeling. The spatial decoupling between the AFm/AFt and CH/gypsum precipitation fronts over several hundreds of microns has also been obtained in other reactive transport simulations of ESA of hydrated cement pastes [47,58–60]. Thermodynamic equilibrium modeling of the titration (i.e. without diffusive transport) of CEM I-based materials by Na_2SO_4 addition has led to the same chemical sequence [7]. SO_4^{2-} ions are first consumed to precipitate ettringite from all types of AFm phases (plus a given amount of portlandite, Eq. 14). In a second stage, SO_4^{2-} ions are consumed to precipitate gypsum at the expense of portlandite (Eq. 15) only once all AFm have been depleted. The HYTEC modeling could have overestimated the separation between the ettringite and gypsum fronts because one single diffusion coefficient and one single porosity were considered in the model. Considering a dual porosity approach where AFm phase are less accessible to SO_4^{2-} by diffusion than portlandite crystals would probably improve the model.

Eventually, the present modeling was able to simulate the migration of the gypsum band that redissolves but enlarges with time, as well as the relative stability of ettringite compared to gypsum during the course of the degradation.

4.2. Consistency between the chemical and mechanical data set

The loss of mechanical properties was related to the decalcification of C-S-H and the dissolution of portlandite, as demonstrated by the measurements and the reactive transport modeling (Fig. 8c). Young's modulus values of less than 5 GPa were measured in the most decalcified zone, in agreement with values of around 3 GPa reported in the literature [55]. This decrease in elastic modulus is consistent with the increase in porosity in the degraded zone, observed both experimentally and numerically. Young's moduli were measured between 15 and 20 GPa at the depth where gypsum precipitation was experimentally observed for both cement pastes. The range of 15-20 GPa is comparable to the Young's moduli obtained in the sound zone.

The higher moduli measured in the C_3A-rich paste is, somehow, supported by the modeling that led to higher ettringite precipitation and lower porosity (Figs. 6 and 7). Thus, despite the difficulty to detect the precipitation of secondary ettringite by SEM-EDS, the presence of ettringite seemed to be highlighted by comparing the Young's moduli obtained experimentally to the ones calculated from the modeling results.

The decrease of porosity due to gypsum formation had probably a greater effect on the global Young's modulus than the relatively high modulus of gypsum (45.7 GPa). A slightly higher Young's modulus was calculated at the gypsum precipitation peak in the C_3A-poor cement paste. In the C_3A-rich cement paste, the consequences of gypsum formation cannot be properly characterized since the amount of gypsum was underestimated in the modeling.

4.3. Impact of gypsum precipitation on expansion and cracking

Paste cracking was systematically observed in the zone of coexistence of gypsum, ettringite and portlandite. This process was observed as well in the study of Planel & al. [51]. The cracking profile suggested that its origin was related to differential internal strains due to a significant swelling initiated by precipitation of expansive products. During the first 6 months, only the C_3A-rich cement pastes showed signs of cracking (Fig. 9). These samples had the highest amount of ettringite as discussed in the previous section. Thus, it could be believed that only ettringite was responsible for the mechanism leading to cracking. However, the experimental results demonstrated that the crack initiation took place in the gypsum formation zone, as also observed by Gollop and Taylor [50] and Planel & al. [51]. Moreover, the C_3A-poor cement paste eventually showed cracking as well after 8 months of degradation, still in the zone of gypsum precipitation (Fig. 11).

As discussed in Sec. 4.1, the formation of gypsum was observed in the portlandite dissolution zone in all samples well before the appearance of massive cracks. Furthermore, Fig. 11 shows cracking which seemed to be generated by an earlier formation of gypsum, which redissolved later to precipitate further inside, close to the decalcification front. The micro-cracks initiated in this later zone of gypsum precipitation were observed. Hence, the precipitation of gypsum would not occur only when the cracks were formed, as suggested by the studies of Yu & al. [4], but before as well. In addition, as portlandite was not completely dissolved in this zone, the available porosity was kept at a low value. Therefore, gypsum crystallization may also contribute to the expansion of cementitious materials if the growth of its crystals takes place in the zones of small-scale porosity which is close to the crystallization pressure theory [61–63].

The amplitude of the stresses may be linked to the volume of the resulting crystals [21,63]. The cracks only found on C_3A-rich cement pastes in the first 6 months would be explained by its higher amount of ettringite precipitation combined to a much higher molar volume of ettringite than gypsum. Thus, the internal swelling pressures may have appeared earlier in the case of C_3A-rich pastes. Inversely, the lower molar volume of gypsum would explain why C_3A-poor cement pastes cracked at 8 months, since a greater quantity of gypsum would be required. This is in agreement with the experiments of El-Hachem & al. [64] in which reducing the amount of C_3A amounts in cement resulted in less cracking but did not ultimately prevent material swelling. Eventually, the occurrence of cracks after only 4 months would suggest that a sufficient mineral precipitation was needed to reach the critical swelling pressure.

Material cracking had probably occurred when a critical volume of formed minerals was reached. Cracking was primarily due to the precipitation of gypsum that exerted a swelling pressure greater than the tensile limit of the cement paste, observed after 4 months for the C_3A-rich cement paste and after 8 months for the C_3A-poor sample (Fig. 9). Cracking represented a preferential pathway for the diffusion of ions and favored the further precipitation of minerals [65]. This would explain why the C_3A-rich cement paste presented such a high quantity of gypsum at 6 months, even greater than that of the C_3A-poor paste. Moreover, the cracking after 6 months had an opening almost 300 times greater than that observed at 4 months. This was possibly due to the abundant precipitation of gypsum, since the facilitated diffusion of SO_4 was reinforced by the cracking itself in addition to porosity increase by decalcification. The overall impact enhanced the sample expansion and the crack aperture, which accelerated the chemo-mechanical degradation. Overall, the comparison of experimental and numerical results highlighted a good agreement between the degradation depths, except for the C_3A-rich sample at 6 months. In the latter case, considering the increase of diffusion coefficient in the cracked zone would have improved the reactive transport modeling [66].

The amount of precipitated ettringite as a function of time is in theory limited to a certain value driven by the quantity of Al available in the cement paste. The precipitation of gypsum depends only on the amounts of Ca and SO_4 available, the former resulting from portlandite dissolution while the latter being possibly more readily supplied by the environment. A higher SO_4 total concentration leads to the precipitation of a larger amount of gypsum [67–69]. In this sense, the amount of gypsum is a marker of the SO_4 concentration which has diffused in the pore solution at a given time. The present experimental results showed larger amounts of gypsum formed with time, suggesting a more important diffusion of SO_4 in the porous media related to the greater decalcification of the material over time. High levels of SO_4 speed up expansion and damage, which hence may be a direct consequence of the greater amount of precipitated gypsum [70].

5. Conclusion

The multiple-technique approach (XRD, SEM-EDS, microtomography, microindentation, and autoradiography) has led to an accurate characterization of the coupled evolution with time of chemical, mineralogical, microstructural and mechanical properties of C_3A-rich and C_3A-poor cement pastes subjected to a weak external sulfate attack (ESA). The wide range of analytical results combined with reactive transport modeling highlighted key processes.

First, there was a significant loss of mechanical properties as the Young's modulus went from 20 GPa in the sound zone to less than 5 GPa in the most degraded zone. This loss of mechanical properties was mostly due to the great increase in porosity induced by portlandite dissolution and C-S-H decalcification, which is mostly driven by a hydrolysis process and not by the ESA strictly speaking.

Secondly, both C_3A-rich and C_3A-poor cement pastes exhibited cracks parallel to the surface exposed to the sulfate solution. However, the onset of cracking was delayed in the case of the C_3A-poor cement paste. Notably, significant damage was observed in the C_3A-rich cement pastes after 6 months of degradation, whereas expansion was evident in the C_3A-poor cement paste only after 8 months. The greater formation of ettringite in the C_3A-rich cement paste, combined with its greater molar volume than that of gypsum, may be responsible for its rapid

expansion. Gypsum would then have to form in greater quantities in the C_3A-poor cement paste to compensate for the lack of ettringite. Sulfate diffusion accelerates during degradation due to greater decalcification, allowing gypsum precipitation to increase over time, while ettringite formation is limited by the paste Al content, leading to expansion and then cracking, which in turn favors mineral precipitation.

Furthermore, cracking was initiated in the zone in which gypsum, secondary ettringite and portlandite were detected. In this area, the porosity was low as portlandite had not fully dissolved and secondary ettringite was formed. Moreover, gypsum precipitation was thermodynamically favored due to the release of Ca^{2+} and the diffusion of SO_4^{2-} ions during the course of the ESA. Therefore, material cracking would have appeared at a time when a critical volume of minerals was formed in the low porosity available, generating swelling pressure. The amount of ettringite was limited by the quantity of aluminum available in the paste, therefore, this critical volume of minerals would have been reached when the amount of gypsum and ettringite was enough to fill the pores and generate swelling pressure.

This study considered sodium sulfate (Na_2SO_4) to emphasize the chemical reactions involving SO_4^{2-} ions (the counter ion Na^+ being weakly reactive). Realizing more sampling over time could enable a closer monitoring of the degradation with time, which would provide more data between the time at which sulfate minerals are formed and when cracking appears. Experimental characterization at a smaller scale has also to be performed to clarify some uncertainties regarding the initiation of swelling pressure by sulfate products formation. Nonetheless, the impact of gypsum formation on cracking should not be neglected, even in a moderately-rich sulfate environment as found in deep geologic nuclear waste disposals.

Acknowledgments

We gratefully acknowledge the reviewers for their relevant comments that greatly helped to increase the clarity of the paper as well as our former colleague, Patrick Le Bescop, now retired from CEA (France), for fruitful discussions.

References

[1] Figg J. Field studies of sulfate attack on concrete. American Ceramic Society, Inc, Materials Science of Concrete: Sulfate Attack Mechanisms (USA),. 1999;315-23.

[2] Tulliani JM, Montanaro L, Negro A, Collepardi M. Sulfate attack of concrete building foundations induced by sewage waters. Cement and Concrete Research. 2002;32(6):843-9.

[3] Santhanam M, Cohen MD, Olek J. Sulfate attack research—whither now? Cement and Concrete Research. 2001;31(6):845-51.

[4] Yu C, Sun W, Scrivener K. Mechanism of expansion of mortars immersed in sodium sulfate solutions. Cement and Concrete Research. 2013;43:105-11.

[5] Gu Y, Martin RP, Metalssi OO, Fen-Chong T, Dangla P. Pore size analyses of cement paste exposed to external sulfate attack and delayed ettringite formation. Cement and Concrete Research. 2019;123:105766.

[6] Neville A. The confused world of sulfate attack on concrete. Cement and Concrete Research. 2004;34(8):1275-96.

[7] Feng P, Garboczi EJ, Miao C, Bullard JW. Microstructural origins of cement paste degradation by external sulfate attack. Construction and Building Materials. 2015;96:391-403.

[8] Ikumi T, Segura I. Numerical assessment of external sulfate attack in concrete structures. A review. Cement and Concrete Research. 2019;121:91-105.

[9] El-Hachem R, Rozière E, Grondin F, Loukili A. Multi-criteria analysis of the mechanism of degradation of Portland cement based mortars exposed to external sulphate attack. Cement and Concrete Research. 2012;42(10):1327-35.

[10] Le Bescop P, Solet C. External sulphate attack by ground water: Experimental study on CEM I cement pastes. Revue européenne de génie civil. 2006;10(9):1127-45.

[11] Yin GJ, Zuo XB, Sun XH, Tang YJ. Macro-microscopically numerical analysis on expansion response of hardened cement paste under external sulfate attack. Construction and Building Materials. 2019;207:600-15.

[12] Flatt RJ, Scherer GW. Thermodynamics of crystallization stresses in DEF. Cement and Concrete Research. 2008;38(3):325-36.

[13] Gu Y, Dangla P, Martin RP, Metalssi OO, Fen-Chong T. Modeling the sulfate attack induced expansion of cementitious materials based on interface-controlled crystal growth mechanisms. Cement and Concrete Research. 2022;152:106676.

[14] Schmidt T, Lothenbach B, Romer M, Neuenschwander J, Scrivener K. Physical and microstructural aspects of sulfate attack on ordinary and limestone blended Portland cements. Cement and Concrete Research. 2009;39(12):1111-21.

[15] Ouyang C, Nanni A, Chang WF. Internal and external sources of sulfate ions in Portland cement mortar: two types of chemical attack. Cement and Concrete Research. 1988;18(5):699-709.

[16] DePuy GW. Chemical resistance of concrete. In: Significance of Tests and Properties of Concrete and Concrete-Making Materials. ASTM International; 1994.

[17] Gonzalez MA, Irassar EF. Ettringite formation in low C3A Portland cement exposed to sodium sulfate solution. Cement and Concrete Research. 1997;27(7):1061-71.

[18] Day RL, Joshi RC. Sulfate Resistance of Mortars Containing Large Proportions of Fly Ash. In: International Seminar on some Aspects of Admixture and Industrial Byproducts on the Durability of Concrete, Götenberg, Sweden. 1986.

[19] Nielsen J. Investigation of resistance of cement paste to sulfate attack. Highway Research Record. 1966;(113).

[20] Wang JG. Sulfate attack on hardened cement paste. Cement and Concrete Research. 1994;24(4):735-42.

[21] Bui NN. Expansion and stresses induced by crystallization in cement-based materials in presence of sulfates [PhD Thesis]. Paris Est; 2016.

[22] Monteiro PJ, Kurtis KE. Experimental asymptotic analysis of expansion of concrete exposed to sulfate attack. ACI Materials Journal. 2008;105(1):62.

[23] Ragoug R, Metalssi OO, Barberon F, Torrenti JM, Roussel N, Divet L, et al. Durability of cement pastes exposed to external sulfate attack and leaching: Physical and chemical aspects. Cement and Concrete Research. 2019;116:134-45.

[24] Tremosa J, Arcos D, Matray JM, Bensenouci F, Gaucher EC, Tournassat C, et al. Geochemical characterization and modelling of the Toarcian/Domerian porewater at the Tournemire underground research laboratory. Applied geochemistry. 2012;27(7):1417-31.

[25] Gaucher EC, Tournassat C, Pearson FJ, Blanc P, Crouzet C, Lerouge C, et al. A robust model for pore-water chemistry of clayrock. Geochimica et Cosmochimica Acta. 2009;73(21):6470-87.

[26] Wersin P, Mazurek M, Gimmi T. Porewater chemistry of Opalinus Clay revisited: Findings from 25 years of data collection at the Mont Terri Rock Laboratory. Applied geochemistry. 2022;138:105234.

[27] Zaier, I., Billiotte, J., De Windt, L., Charmoille, A. The impact of common impurities present in gypsum deposits on in situ dissolution kinetics. Environmental Earth Sciences. 2023:82(1), 31.

[28] Bellmann, F., Erfurt, W., Ludwig, H. M. Field performance of concrete exposed to sulphate and low pH conditions from natural and industrial sources. Cement and Concrete Composites. 2012:34(1), 86-93.

[29] Mehta PK. Mechanism of sulfate attack on portland cement concrete—Another look. Cement and Concrete Research. 1983;13(3):401-6.

[30] Qin S, Zou D, Liu T, Jivkov A. A chemo-transport-damage model for concrete under external sulfate attack. Cement and Concrete Research. 2020;132:106048.

[31] Pouya J, Neji M, De Windt L, Péralès F, Socié A, Corvisier J. Mineralogical Evolution and Expansion of Cement Pastes in a Sulfate-Confined Environment. Minerals. 2023; 13(1):1.

[32] Barbieri-Albert B. Altération de matrices cimentaires par des eaux de pluie et des eaux sulfatées. Approche expérimentale et thermodynamique [PhD Thesis]. Ecole Nationale Supérieure des Mines de Saint-Etienne; 2002.

[33] Le Saout G, Füllmann T, Kocaba V, Scrivener K. Quantitative study of cementitious materials by X-ray diffraction/Rietveld analysis using an external standard. In: 12th International congress on the chemistry of cement Montréal, Canada. 2007.

[34] Vaitkus A, Merkys A, Gražulis S. Validation of the crystallography open database using the crystallographic information framework. Journal of Applied Crystallography. 2021;54(2).

[35] Hartigan JA, Wong MA. Algorithm AS 136: A k-means clustering algorithm. Journal of the royal statistical society series c (applied statistics). 1979;28(1):100-8.

[36] Weitkamp T, Scheel M, Giorgetta JL, Joyet V, Le Roux V, Cauchon G, et al. The tomography beamline ANATOMIX at Synchrotron SOLEIL. In: Journal of Physics: Conference Series. IOP Publishing; 2017. p. 012037.

[37] Oliver WC, Pharr GM. An improved technique for determining hardness and elastic modulus using load and displacement sensing indentation experiments. Journal of Materials Research. 1992;7(6):1564-83.

[38] Constantinides G, Chandran KR, Ulm FJ, Van Vliet KJ. Grid indentation analysis of composite microstructure and mechanics: Principles and validation. Materials Science and Engineering: A. 2006;430(1-2):189-202.

[39] Gaboreau S, Prêt D, Tinseau E, Claret F, Pellegrini D, Stammose D. 15 years of in situ cement–argillite interaction from Tournemire URL: Characterisation of the multi-scale spatial heterogeneities of pore space evolution. Applied Geochemistry. 2011;26(12):2159-71.

[40] Robinet JC, Sardini P, Siitari-Kauppi M, Prêt D, Yven B. Upscaling the porosity of the Callovo-Oxfordian mudstone from the pore scale to the formation scale; insights from the 3H-PMMA autoradiography technique and SEM BSE imaging. Sedimentary Geology. 2015;321:1-10.

[41] Sammaljärvi J, Rama MS, Ikonen J, Muuri E, Hellmuth KH, Siitari-Kauppi M. Free radical polymerisation of methacrylates with thermal initiator in clay rock. Engineering Geology. 2016;210:70-83.

[42] van Der Lee J, De Windt L, Lagneau V, Goblet P. Module-oriented modeling of reactive transport with HYTEC. Computers & Geosciences. 2003;29(3):265-75.

[43] De Windt L, Devillers P. Modeling the degradation of Portland cement pastes by biogenic organic acids. Cement and Concrete Research. 2010;40(8):1165-74.

[44] Blanc P, Lassin A, Piantone P, Azaroual M, Jacquemet N, Fabbri A, et al. Thermoddem: A geochemical database focused on low temperature water/rock interactions and waste materials. Applied Geochemistry. 2012;27(10):2107-16.

[45] Haecker CJ, Garboczi EJ, Bullard JW, Bohn RB, Sun Z, Shah SP, et al. Modeling the linear elastic properties of Portland cement paste. Cement and Concrete Research. 1 oct 2005;35(10):1948-60.

[46] Parrot LJ. Prediction of cement hydration. In: Proceedings of the British Ceramic Society. 1984. p. 41-53.

[47] Soive A, Roziere E, Loukili A. Parametrical study of the cementitious materials degradation under external sulfate attack through numerical modeling. Construction and Building Materials. 2016;112:267-75.

[48] Richet et Ayache C. Solubilité, diffusion et sorption des émetteurs alpha et Beta gamma dans les liants hydrauliques. NT SESD-CEA, 96-39; 1996.

[49] Mori T, Tanaka K. Average stress in matrix and average elastic energy of materials with misfitting inclusions. Acta Metallurgica. 1973;21(5):571-4.

[50] Gollop RS, Taylor HFW. Microstructural and microanalytical studies of sulfate attack. I. Ordinary Portland cement paste. Cement and Concrete Research. 1992;22(6):1027-38.

[51] Planel D, Sercombe J, Le Bescop P, Adenot F, Torrenti JM. Long-term performance of cement paste during combined calcium leaching–sulfate attack: kinetics and size effect. Cement and Concrete Research. 2006;36(1):137-43.

[52] Lothenbach, B., Pelletier-Chaignat, L., Winnefeld, F. Stability in the system CaO–Al2O3–H2O. Cement and concrete research. 2012;42(12):1621-1634.

[53] Jennings HM, Tennis PD. Model for the developing microstructure in Portland cement pastes. Journal of the American Ceramic Society. 1994;77(12):3161-72.

[54] Socié, A., Dubois, F., Monerie, Y., Neji, M., & Perales, F. Simulation of internal and external sulfate attacks of concrete with a generic reactive transport-poromechanical model. European Journal of Environmental and Civil Engineering. 2023; 27(12), 3679-3706.

[55] Constantinides G, Ulm FJ. The effect of two types of CSH on the elasticity of cement-based materials: Results from nanoindentation and micromechanical modeling. Cement and Concrete Research. 2004;34(1):67-80.

[56] Stora E, Bary B, He QC, Deville E, Montarnal P. Modelling and simulations of the chemo–mechanical behaviour of leached cement-based materials: leaching process and induced loss of stiffness. Cement and Concrete Research. 2009;39(9):763-72.

[57] Damidot et Glasser. Thermodynamic investigation of the CaO-Al2O3-CaSO4-H2O syste at 25°C and influence of Na2O. Cement and Concrete Research. 1993;25:221-38.

[58] Planel D. Les effets couplés de la précipitation d'espèces secondaires sur le comportement mécanique et la dégradation chimique des bétons. PhD Thesis, Univ. Paris Est ; 2002.

[59] Lothenbach B, Bary B, Le Bescop P, Schmidt T, Leterrier N. Sulfate ingress in Portland cement. Cement and Concrete Research. 1 août 2010;40(8):1211-25.

[60] Bary B, Leterrier N, Deville E, Le Bescop P. Coupled chemo-transport-mechanical modelling and numerical simulation of external sulfate attack in mortar. Cement and Concrete Composites. 1 mai 2014;49:70-83.

[61] Scherer GW. Crystallization in pores. Cement and Concrete research. 1999;29(8):1347-58.

[62] Flatt RJ. Salt damage in porous materials: how high supersaturations are generated. Journal of crystal growth. 2002;242(3-4):435-54.

[63] Derluyn, H., Moonen, P., Carmeliet, J., Deformation and damage due to drying-induced salt crystallization in porous limestone. Journal of the Mechanics and Physics of Solids 2014; 63, 242–255. https://doi.org/10.1016/j.jmps.2013.09.005

[64] El-Hachem R, Rozière E, Grondin F, Loukili A. New procedure to investigate external sulphate attack on cementitious materials. Cement and Concrete Composites. 2012;34(3):357-64.

[65] Socié A, Dubois F, Monerie Y, Perales F. Multibody approach for reactive transport modeling in discontinuous-heterogeneous porous media. Computational Geosciences. 2021;25(5):1473-91.

[66] Seigneur N, De Windt L, Poyet S, Socié A, Dauzères A. Modelling of the evolving contributions of gas transport, cracks and chemical kinetics during atmospheric carbonation of hydrated C3S and C-S-H pastes. Cement and Concrete Research. 2022;160:106906.

[67] Irassar EF, Bonavetti VL, Gonzalez M. Microstructural study of sulfate attack on ordinary and limestone Portland cements at ambient temperature. Cement and Concrete Research. 2003;33(1):31-41.

[68] Bellmann F, Möser B, Stark J. Influence of sulfate solution concentration on the formation of gypsum in sulfate resistance test specimen. Cement and Concrete Research. 2006;36(2):358-63.

[69] Müllauer W, Beddoe RE, Heinz D. Sulfate attack expansion mechanisms. Cement and Concrete Research. 2013;52:208-15.

[70] Schmidt T. Sulfate attack and the role of internal carbonate on the formation of thaumasite. EPFL; 2007.